# Seismic structure and magmatic construction of crust at the ultraslow-spreading Southwest Indian Ridge at 50°28'E

Hanchao Jian, Yongshun John Chen, Satish C. Singh, Jiabiao Li, Minghui Zhao, Aiguo Ruan, Xuelin Qiu

▶ **To cite this version:**

Hanchao Jian, Yongshun John Chen, Satish C. Singh, Jiabiao Li, Minghui Zhao, et al.. Seismic structure and magmatic construction of crust at the ultraslow-spreading Southwest Indian Ridge at 50°28'E. Journal of Geophysical Research : Solid Earth, 2017, 122, pp.18-42. 10.1002/2016JB013377 . insu-03748882

**HAL Id: insu-03748882**
**https://insu.hal.science/insu-03748882**

Submitted on 10 Aug 2022

**HAL** is a multi-disciplinary open access archive for the deposit and dissemination of scientific research documents, whether they are published or not. The documents may come from teaching and research institutions in France or abroad, or from public or private research centers.

L'archive ouverte pluridisciplinaire **HAL**, est destinée au dépôt et à la diffusion de documents scientifiques de niveau recherche, publiés ou non, émanant des établissements d'enseignement et de recherche français ou étrangers, des laboratoires publics ou privés.

Copyright

AGU PUBLICATIONS

JGR

Journal of Geophysical Research: Solid Earth

RESEARCH ARTICLE
10.1002/2016JB013377

**Key Points:**
- A three-dimensional crustal structure of an ultraslow-spreading segment indicates excess melt supply
- The magmatic segment is fed by the melt redistributed from the magma chamber at the segment center
- The oblique spreading has strong effects on the magmatism in the crust

**Supporting Information:**
- Supporting Information S1

**Correspondence to:**
Y. J. Chen,
johnyc@pku.edu.cn

**Citation:**
Jian, H., Y. J. Chen, S. C. Singh, J. Li, M. Zhao, A. Ruan, and X. Qiu (2017), Seismic structure and magmatic construction of crust at the ultraslow-spreading Southwest Indian Ridge at 50°28′E, *J. Geophys. Res. Solid Earth*, *122*, 18–42, doi:10.1002/2016JB013377.

Received 21 JUL 2016
Accepted 11 NOV 2016
Accepted article online 17 NOV 2016
Published online 12 JAN 2017

©2016. American Geophysical Union. All Rights Reserved.

# Seismic structure and magmatic construction of crust at the ultraslow-spreading Southwest Indian Ridge at 50°28′E

**Hanchao Jian[1,2], Yongshun John Chen[1,3], Satish C. Singh[2], Jiabiao Li[4], Minghui Zhao[5], Aiguo Ruan[4], and Xuelin Qiu[5]**

[1]Institute of Theoretical and Applied Geophysics, School of Earth and Space Science, Peking University, Beijing, China, [2]Laboratoire de Géosciences Marines, Institut de Physique du Globe de Paris, Paris, France, [3]School of Oceanography, South University of Science and Technology of China, Shenzhen, China, [4]Second Institute of Oceanography, State Oceanic Administration, Hangzhou, China, [5]South China Sea Institute of Oceanology, Chinese Academy of Sciences, Guangzhou, China

**Abstract** We present a three-dimensional crustal structure of a magmatically robust segment of the ultraslow-spreading Southwest Indian Ridge at 50°28′E based on tomographic inversions of an ocean bottom seismometer data set. Our results show an upper crustal low-velocity band in the axial zone, which is attributed to increased porosities due to active extensions, leading to anisotropy in the upper crust with a fast direction subperpendicular to the spreading direction. In the lower crust, the results reveal a round-shaped low-velocity anomaly at the segment center, indicative of high temperatures and/or a small amount of melt, suggestive of the presence of an axial magma chamber. At the midcrustal depth, an along-axis asymmetry is observed with respect to the segment center. While a small low-velocity anomaly indicates lateral magma redistribution toward the western segment end, the deep-penetrating low velocities and high velocity gradients toward the eastern end suggest that the crust is colder and contains a thicker fractured layer. This asymmetry occurs very close to the axial magma chamber (<5 km) and seems to be related to the fact that the oblique-spreading domain at the eastern end offsets the ridge axis by a larger distance than that at the western end. We suggest that an along-axis deep-penetrating hydrothermal circulation develops on the east side of the axial magma chamber, in response to the rapid change from orthogonal- to oblique-spreading domains and cools the crust.

## 1. Introduction

The crustal accretion at mid-ocean ridges (MOR) as a combination of the tectonic extension and the magmatic construction depends on the spreading rates. At fast-spreading ridges, the magmatism is robust and relatively uniform along the ridge axis and creates a continuous axial rise except at transform faults and several large overlapping spreading centers [*Macdonald et al.*, 1988; *Carbotte et al.*, 2015]. This is confirmed by seismic observations revealing the continuous distribution of axial melt lenses along the ridge axis [e.g., *Kent et al.*, 2000; *Carbotte et al.*, 2013], underlain by a broad melt anomaly in the lower crust [*Vera et al.*, 1990; *Dunn et al.*, 2000; *Harding et al.*, 1989]. When the spreading rate and/or the overall melt supply decreases, the magmatic construction shows a more three-dimensional (3-D) and short-term variability. For instance, at the slow-spreading Mid-Atlantic Ridge (MAR), the ridge axis is partitioned into tens of kilometer long segments by transform or nontransform offsets. Within each segment, there is a magmatic center dominated by a higher topography and a lower mantle Bouguer gravity anomaly (MBA) [e.g., *Lin et al.*, 1990; *Escartin et al.*, 2001]. Seismic studies have shown the presence of a lower crustal magma chamber [*Seher et al.*, 2010a; *Dunn et al.*, 2005], sometimes overlain by an axial melt lens [*Singh et al.*, 2006], confined beneath the segment center, suggesting a focused melt delivery from the mantle. This melt could be injected vertically or redistributed along the ridge axis to feed the whole ridge segment [e.g., *Hooft et al.*, 2000; *Barclay et al.*, 2001; *Seher et al.*, 2010a].

The bathymetry has revealed a much different pattern of along-axis variations at the ultraslow-spreading ridges with full-spreading rates below 20 mm/yr, including the Southwest Indian Ridge (SWIR) and the Arctic ridge system. For instance, along the SWIR, the relatively orthogonal-spreading magmatic centers are narrower and widely spaced as compared to those at slow-spreading ridges. They are mostly connected by

elongated deep domains, which are spreading obliquely and have lengths comparable to or even larger than the magmatic centers [*Dick et al.*, 2003; *Sauter et al.*, 2001; *Mendel et al.*, 1997]. These deep domains were first recognized as nontransform discontinuities (NTD) [e.g., *Rommevaux-Jestin et al.*, 1997; *Mendel et al.*, 1997]. Lately, certain authors have argued that some long-stretch NTDs represent a novel class of amagmatic spreading segments, as vast mantle-derived peridotites are exposed on the smooth seafloor with only scattered basalts at the center of these deep domains [*Dick et al.*, 2003; *Cannat et al.*, 2006; *Sauter et al.*, 2013]. The MBA variation generally agrees with the bathymetry, with low MBA values beneath high-topography magmatic centers, indicating lighter crustal and upper mantle materials and/or a thicker crust, and thus more melt supply, which quickly diminishes toward the NTD [*Cannat et al.*, 1999]. *Dick et al.* [2003] suggested that the oblique spreading suppresses the melt generation in the mantle by reducing the effective spreading rate, whereas *Cannat et al.* [2008] proposed that it has more effects on the crustal-level magma redistribution from the magmatic centers. However, the details of the magmatic accretion and its link to the amagmatic accretion have been poorly understood due to the lack of high-resolution seismic images.

Accompanying the magmatism, hydrothermal activity has been extensively observed at fast- and slow-spreading ridges [*Baker*, 2009] and began to be detected at ultraslow ridges recently. It seems that the frequency of hydrothermal venting (number of sites per ridge length) is linearly correlated with the spreading rate and hence the long-term melt supply [*Baker et al.*, 2004]. However, considering the limited percentage of seafloor associated with magmatism at the ultraslow ridges, they are more efficient than faster-spreading ridges in supporting hydrothermal vent fields [*Baker et al.*, 2004]. Since the first active hydrothermal vent at the SWIR was confirmed in 2007 [*Tao et al.*, 2012], more vent fields have been discovered in the previously unexplored ridge portions (https://vents-data.interridge.org/ventfields). A unique relationship between the magma system and hydrothermal activity is expected for the ultraslow ridges, which also requires insights from seismic images.

In order to better understand the ultraslow-spreading processes, an active-source ocean bottom seismometer (OBS) experiment was conducted at the SWIR segments 28 and 27 (after the nomenclature of *Cannat et al.* [1999]), between 49°50′E and 50°50′E [*Li et al.*, 2015; *Zhao et al.*, 2013; *Niu et al.*, 2015], where one of the shallowest axial volcanoes of the SWIR is present. These two segments also host two hydrothermal vent fields [*Tao et al.*, 2012]. In this paper, we present the tomographic analysis of the OBS data set acquired along segment 27. A three-dimensional (3-D) crustal velocity structure is constrained using the traveltimes of crustal refraction (Pg) arrivals and Moho reflection (PmP) arrivals.

## 2. Geological Background

The mantle upwelling models that successfully fit the observations at fast- and slow-spreading ridges predict a dramatic decrease in the magmatic component of the crustal accretion under the ultraslow-spreading rate, due to enhanced conductive cooling [*Reid and Jackson*, 1981; *Bown and White*, 1994; *White et al.*, 2001]. However, the analyses of seafloor morphology, gravity, and geochemistry indicate significant large-scale variations of melt supply along the SWIR [*Cannat et al.*, 2008; *Sauter and Cannat*, 2010], despite the almost constant full-spreading rate of ~13 mm/yr [*DeMets et al.*, 2015]. To the west of the Andrew Bain fracture zone (FZ) at ~30°E and to the east of the Melville FZ at ~60°E, these two ridge sections are characterized by deep axial valleys and high MBA. Widely spaced magmatic centers are connected by long-distance oblique-spreading domains with vast exposure of mantle-derived peridotites [*Dick et al.*, 2003; *Cannat et al.*, 2006; *Sauter et al.*, 2013]. Comparing to the slow-spreading MAR, the seamounts are fewer but taller [*Mendel and Sauter*, 1997]. They have been suggested to represent the end-member of magma-poor spreading environments, which may be due to lower mantle temperatures and/or a depleted mantle beneath the ultraslow-spreading ridge [*Cannat et al.*, 2008].

On the other hand, the level of melt supply is higher at the central portion of the SWIR [*Sauter and Cannat*, 2010]. Between the Indomed FZ and Gallieni FZ (Figure 1a), the regional average axial depth is >1000 m shallower than the easternmost portion [*Cannat et al.*, 2008]. Most dredges in this area found basaltic samples from the axial valley [*Zhou and Dick*, 2013]. Lower values of the MBA and Na8.0 contents also suggest a relatively robust melt supply, whereas the off-axis bathymetric swell suggests that this melt supply may have been lasting for about 10 Ma [*Sauter et al.*, 2009]. The seamounts and axial volcanic ridges are more densely distributed. The oblique-spreading NTDs within this region have a total stretch comparable to the relatively orthogonal-spreading magmatic centers and orientate the ridge axis with an overall obliquity of ~25° [*Cannat et al.*, 2008].

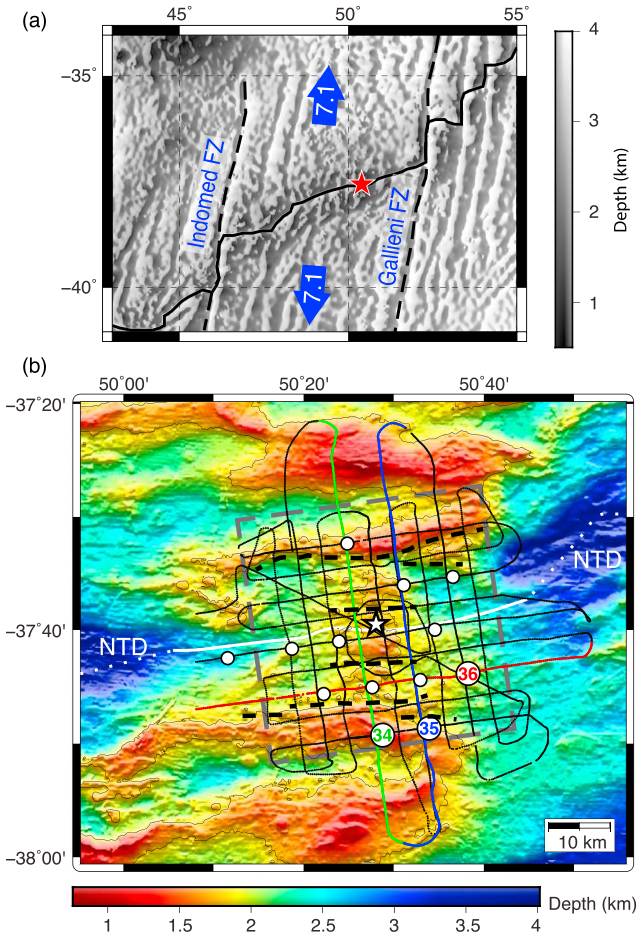


**Figure 1.** Bathymetry and the seismic survey. (a) Regional map showing the SWIR ridge axis (black curve) between the Indomed and Gallieni fracture zones (FZ), whose trajectories are shown as dashed black curves. The red star marks the study area shown in Figure 1b. The blue arrows with numbers show the spreading direction and half-spreading rate in mm/yr [*DeMets et al.*, 1994]. (b) The local bathymetry map and seismic experiment layout. The white curves are the ridge axis of segment 27 (solid) and nontransform discontinuities (NTD, dashed). The black dashed curves are bounding faults, and the white star is an extinct hydrothermal vent [*Tao et al.*, 2012]. The bathymetry is contoured at 1.8 km. The dotted curves and white circles mark the shot and OBS locations, respectively. The OBS corresponding to the data shown in Figure 2 is labeled with numbers, in the same color as the corresponding shots. The gray dashed box outlines the central area of the model shown in Figures 4 and 7.

The shallowest axial volcano (<1500 m depth) in this section lies at the center of segment 27 (Figure 1b), where the MBA is as low as −84 mGal [*Sauter et al.*, 2001], indicating a thicker crust. Besides, *Sauter et al.* [2004] observed a low-magnetization anomaly at this segment center and suggested that the lava is not highly fractionated because of high magmatic activity. On the west and east sides, this segment is bound by two NTDs that offset the ridge axis by <10 km and 18 km, respectively [*Sauter et al.*, 2001]. Correspondingly, the western NTD basin is shorter, shallower, and less oblique than the eastern one. The along-axis MBA variation is also much steeper toward the eastern segment end than toward the western one, which led *Sauter et al.* [2001] to suggest that segment 28 lying next to the western NTD may be fed by the laterally redistributed magma from segment 27. While segment 28 hosts an active hydrothermal vent field, segment 27 has a large amount of sulfide deposits at its center indicating a vent field that recently ceased [*Tao et al.*, 2012].

## 3. Seismic Experiment and Data Processing

### 3.1. Seismic Experiment and Data

The OBS experiment covered two 3-D survey areas, centered at the center of segment 27 and the western end of segment 28, respectively, and connected by a two-dimensional (2-D) profile [*Li et al.*, 2015; *Zhao et al.*, 2013]. This paper presents the analysis of the seismic data at segment 27 (Figure 1a). Thirteen OBSs used in

this tomographic analysis were deployed within a circular area with a diameter of ~35 km and had a sampling interval of 4 ms. We used an array of four air guns with a total volume of 98.32 L as a source, which was towed at a nominal depth of 10 m and navigated using shipboard GPS. It was fired at a spacing of ~240 m along a grid of shooting lines spaced at ~4 km. Nine shooting lines were aligned parallel to the ridge axis, while nine lines were perpendicular to the ridge axis. There was also one line diagonal to the study area and a circular profile with a 17 km diameter at the center of the study area (Figure 1b). A total of 5765 shots were fired. Eleven OBS registered seismic signals from all these shots, while the other two only registered signals from half of the shots due to an unexpected failure.

Three types of primary seismic phases were recorded including direct water waves, crustal *P* wave refractions (Pg) and crust-mantle boundary (Moho) *P* wave reflections (PmP) (Figure 2). After correcting for the water path to remove the influence of seafloor topography [*Purdy*, 1982], we can easily identify different seismic arrivals based on the offset and moveout. The Pg arrivals are observed to a maximum offset of about 50 km as the first arrivals. The Pg waveforms, whose ray path penetrates down to the lower crust near the segment center, are strongly attenuated to form a "shadow zone" (Figure 2a). It may be indicative of a lower crustal low-velocity anomaly (LVA). However, there are other OBS records that show a continuous Pg arrival without any shadow zone (Figure 2d). The nearest PmP reflections arrive at ~25 km offset after the shadow zone. However, the Pn phase is rarely observed in the data set, although the maximum source-receiver offset is >50 km. The presence of extra long offsets for Pg phases as compared to the seismic observations from the MAR [e.g., *Dunn et al.*, 2005; *Seher et al.*, 2010a] indicates the possibility of a thicker crust in this region.

### 3.2. OBS Data Processing and Picking

The prepicking processing of seismic data includes the determination of the shot and OBS times and positions. The shot times and positions were determined using the onboard GPS, with a correction for the distance between the GPS antenna and the center of the air gun array based on the heading direction [*Ao et al.*, 2010]. The seismic data were also corrected for the OBS clock drift by comparing the internal clock and the GPS time before deployment and after recovery, assuming a linear clock drift. Then we relocated the OBS by inverting the traveltimes of direct arrivals for OBS locations, as well as the water column velocity and a delay time for each instrument. This method has been widely used in the OBS data processing [*Bazin et al.*, 2001; *Creager and Dorman*, 1982; *Seher et al.*, 2010a; *Toomey et al.*, 1994]. For every individual instrument, we picked the direct-arrival traveltimes at offsets up to 15–20 km, and the root-mean-square (RMS) of residuals was reduced to 4–7 ms, less than two sampling intervals. The inverted water column velocity is 1502±2 m/s. All instruments roughly drifted ~1 km to the east, indicating little variations of current during the experiment.

We semiautomatically picked the Pg and PmP arrivals after applying a zero-phase filter with a pass band between 3 and 8 Hz. We picked the arrival at its maximum peak and then shifted the picked time to the first break with a constant time that was estimated from the stacked signature for each pair of the OBS and the shooting line. The uncertainties of traveltimes are associated with the errors in the shot position (5 ms), OBS location (6 ms), bathymetry (10 ms), ray tracing (8 ms), and traveltime picking. We estimated the uncertainty associated with the picking by using the cross-correlation coefficient between the picked arrival and the stacked signature as a proxy. Their relationships were derived by fitting the results from statistical experiments. Finally, we picked the traveltimes for 50,228 Pg and 4563 PmP arrivals. The RMS value of picking uncertainties is 32 ms for Pg and 46 ms for PmP.

### 3.3. Traveltime Tomography

We performed the traveltime tomography by adopting the iterative inversion method of *Van Avendonk et al.* [1998, 2004]. In the ray tracing, the slowness model is parameterized on a regular 3-D grid including a water layer on the top, and the interfaces are defined on a regular grid of depth nodes, whose horizontal positions are coincident with those of the slowness grid. The algorithm uses a shortest-path method to find the global minimum of traveltimes in an arbitrary media and its ray path. It can also model secondary arrivals associated with an interface by forcing ray paths traveling through an interface point [*Moser*, 1991]. The grid spacing of 200 m horizontally and 75 m vertically is sufficient to predict the traveltimes with an error less than 8 ms for this study. The model volume is $73.8 \times 73.8 \times 13.95$ km$^3$, corresponding to $370 \times 370 \times 187$ nodes.

The perturbation model in the inversion is defined on a grid with a horizontal spacing of 600 m and a vertical spacing that is 150 m in the upper 4.8 km and gradually increases to 300 m at the bottom of the model.

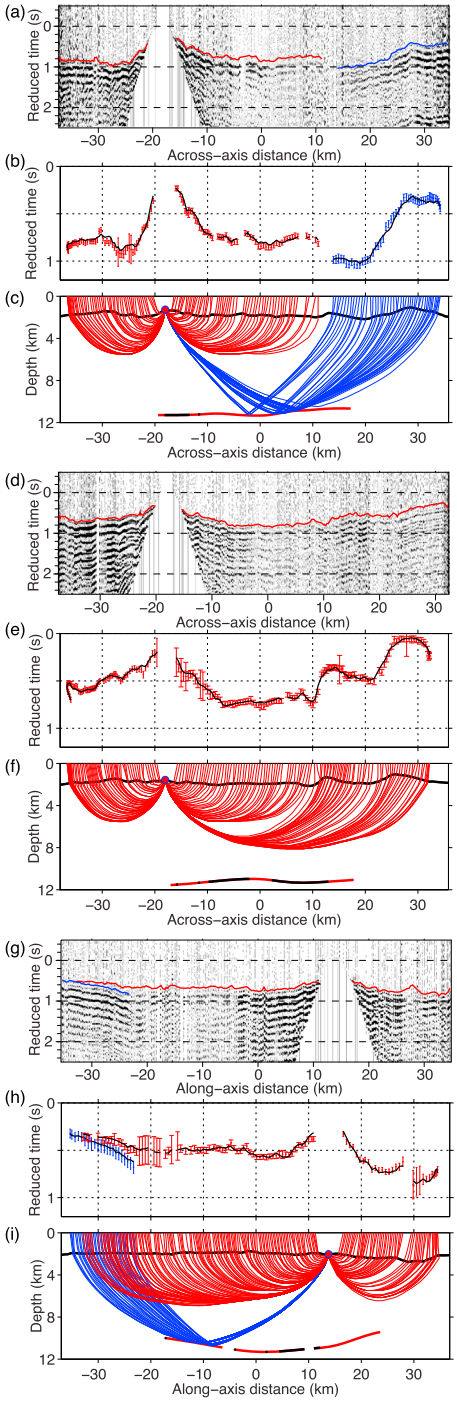


**Figure 2.** Seismic data and ray path examples. The record gathered by OBS 34 from the shooting profile running across the ridge axis directly over it. Their locations are marked in Figure 1b. (a) The OBS data processed for display purpose. The data were first multiplied with time to compensate for the geometrical spreading. A zero-phase band-pass filter with a pass band between 3 and 8 Hz was applied to suppress noise. The time axis was reduced with a velocity of 6.5 km/s and corrected for the seafloor topography. Finally, the water wave was muted. Overlying the wiggles, the red and blue curves show picked times of Pg and PmP arrivals, respectively. (b) Comparison of the picked traveltimes and the predictions from the inverted model (the standard solution, see section 4.2 for details). The error bars represent the picked data with the length representing the uncertainties. The black curves show the corresponding predictions that were calculated with the ray paths shown in Figure 2c. (c) The corresponding ray paths. The seafloor and the Moho interface are marked as boundaries of the crust. Along the Moho interface, the red color indicates the PmP reflecting points from the whole data set. The data and ray path have been decimated by a factor of 2 for clarity. (d–f) Similar to Figures 2a–2c but for OBS 35; (g–i) Similar to Figures 2a–2c but for OBS 36.

The misfit function is minimized using a LSQR method [*Paige and Saunders*, 1982] in a least squares sense, which includes the traveltime data misfits and the model roughness:

$$F = \left\| \begin{array}{c} \mathbf{C}_d^{-1}\left(\mathbf{A}\delta\mathbf{m} - \delta\mathbf{d}\right) \\ \varepsilon\mathbf{I}\delta\mathbf{m} \\ \lambda_u\mathbf{R}\left(\mathbf{m}_u + \delta\mathbf{m}_u\right) \\ \lambda_i\mathbf{R}\left(\mathbf{m}_i + \delta\mathbf{m}_i\right) \end{array} \right\|^2 . \quad (1)$$

Here $\delta\mathbf{d}$ is the traveltime data residual for the current model. $\mathbf{A}$ is a matrix containing the Fréchet derivatives of traveltime data with respect to the model $\mathbf{m}$. $\mathbf{C}_d$ is a diagonal matrix composed of the picking uncertainties. $\mathbf{I}$ is a unit matrix and $\varepsilon$ is a damping factor. $\mathbf{R}$ is a 3-D or 2-D Laplace operator, which imposes smoothing constraints on the slowness model ($\mathbf{m}_u$) or the interface depth model ($\mathbf{m}_i$), weighted by the regularization parameters $\lambda_u$ and $\lambda_i$, respectively. $\lambda_u$ can be different for the smoothing constraints along the horizontal and vertical directions. The smoothing operator is applied to the updated model instead of the model perturbation, to reduce the bias toward the starting model [*McCaughey and Singh*, 1997; *Shaw and Orcutt*, 1985; *Van Avendonk et al.*, 2004].

We inverted for the slowness and interface depth simultaneously. Their units and magnitudes are different, so the inversion via an iterative matrix solver like LSQR could be biased [*Hobro et al.*, 2003; *Korenaga et al.*, 2000; *McCaughey and Singh*, 1997]. To mitigate this multiparameter issue, we used a normalization method similar to *Dunn et al.* [2005] and *Korenaga et al.* [2000]. During the inversion, the two types of model parameters were normalized by model uncertainties ($\sigma_i$ for the interface depth and $\sigma_u$ for the slowness):

$$\mathbf{m} = \begin{bmatrix} \sigma_u^{-1} & 0 \\ 0 & \sigma_i^{-1} \end{bmatrix} \begin{bmatrix} \mathbf{m}_u \\ \mathbf{m}_i \end{bmatrix} . \quad (2)$$

Correspondingly, the Fréchet derivative $\mathbf{A}$ was normalized to keep $\mathbf{A}\delta\mathbf{m}$ unchanged. Hence, all the model parameters involved in the objective function (equation (1)) were dimensionless. The inverse of the model uncertainties would also control the strength of damping constraints on the slowness and the interface depth perturbations. A smaller value of $\sigma_u$ or $\sigma_i$ would lead to stronger damping constraints on the slowness or on the interface depth, respectively.

The data fitting was quantified using $\chi^2$, denoting the mean square of residuals normalized by the picking uncertainty. A $\chi^2$ value close to 1 would indicate a data fitting around the assigned uncertainties. The overall strength of regularization (damping and smoothing) was tuned using a secant method to reach a target of $\chi^2$ for each iteration, which was specified to decrease gradually and to keep the localized linear search method valid [*Van Avendonk et al.*, 1998]. The damping was removed when the data fitting was almost complete ($\chi^2 < 2$). Then the jumping technique was applied to seek the smoothest model among the models that can equally fit the data [*Shaw and Orcutt*, 1985]. Finally, we examined the resolvability through checkerboard tests.

## 4. Results

### 4.1. Construction of the Starting Model

The choice of the starting model is essential for a nonlinear inverse problem. A general way is to generate a 1-D starting model from previous studies in the same area or similar areas [*Seher et al.*, 2010a]. However, the gravimetric observations [*Sauter et al.*, 2009] at this study area suggest that the crustal thickness is more than the global average of ~6 km [*Chen*, 1992], much larger than any other seismically studied segments at ultraslow-spreading ridges [*Jokat et al.*, 2012; *Minshull et al.*, 2006]. As the morphology shows a similarity to the slow-spreading segments, we first constructed a velocity-depth profile similar to the MAR type velocity profiles at segment centers [*Canales et al.*, 2000a; *Hooft et al.*, 2000; *Seher et al.*, 2010a]. It was hung on the seafloor to construct a 3-D starting model for first-arrival tomography, which was run with strong smoothing constraints to fit only the Pg traveltimes. An updated 1-D velocity profile was then obtained by averaging the inverted model. We then hung the new 1-D velocity model on the seafloor and included a Moho interface at 10 km below sea level (bsl) to create the 3-D starting model. This starting model produced an RMS residual of 100 ms for Pg and 105 ms for PmP, and an overall $\chi^2$ of 12.6 (Figure 3).

### 4.2. On the Velocity-Depth Trade-Off

In oceanic crustal studies, the nonuniqueness of the inversion arises from the trade-off between the lower crustal velocity and the Moho depth. This is because the very small or absence of vertical velocity gradients

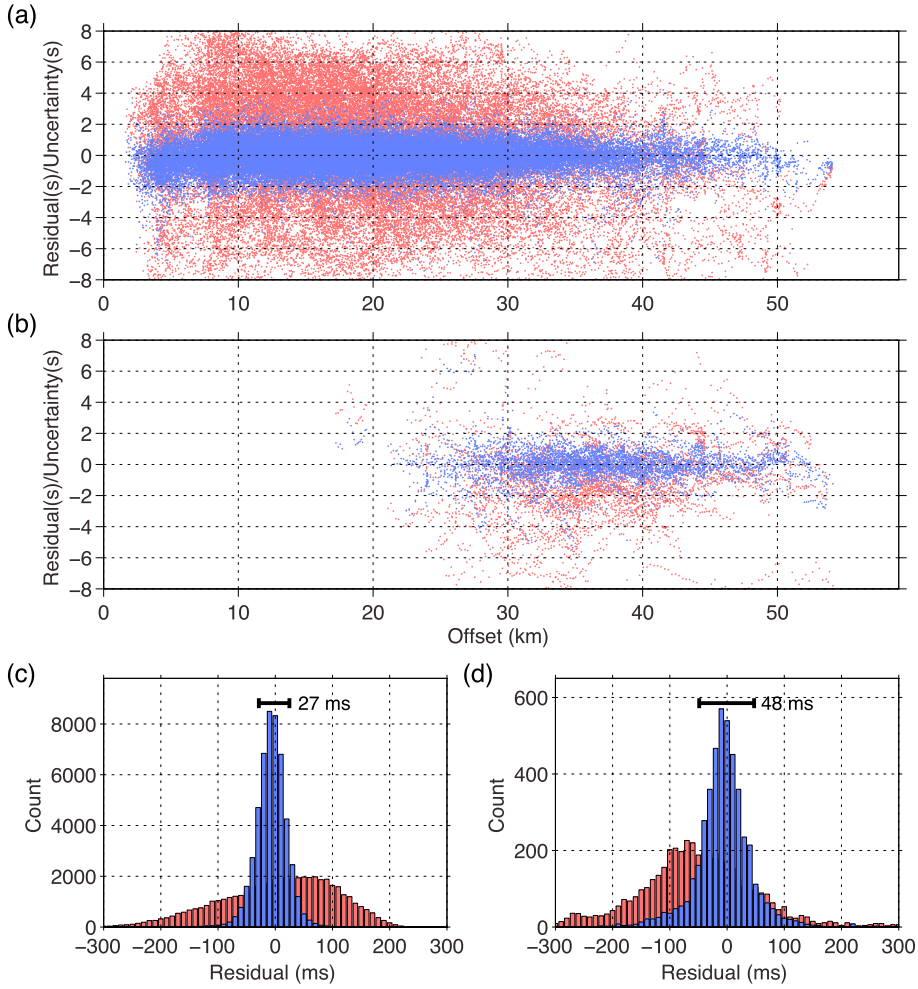


**Figure 3.** Normalized residuals versus source-receiver offsets from the starting model (red color) and the inverted model (blue color) for (a) Pg arrivals and (b) PmP arrivals. Histogram of the absolute residual values for (c) Pg arrivals and (d) PmP arrivals. The normalized residual is the difference between the observed and predicted traveltimes divided by the picking uncertainty. The horizontal error bars in Figures 3c and 3d mark the standard deviation. The RMS of the normalized residuals from the inverted model is close to unity for both phases.

in the lower crust prohibits Pg sampling the lowest crust. In the profiles running over the segment center, the PmP arrivals can be picked at relatively small offsets, but the Pg amplitudes are strongly reduced and not identifiable at long offsets (Figure 2a). Hence, the PmP reflections are used to constrain both the lower crustal velocity and the Moho interface depth structure, and there are no Pn arrivals to constrain the upper mantle. The resolution of gravity is not good enough to resolve the ambiguity. Therefore, we assess the velocity-depth ambiguity via exploring the solution space with different regularization parameters and inversion procedures [*Dunn et al.*, 2005; *Korenaga et al.*, 2000; *Seher et al.*, 2010a].

In the framework of the regularized inversion, the $\sigma_i^{-1}/\sigma_u^{-1}$ ratio controls the relative strength of damping constraints on the interface depth structure with respect to the slowness structure. The $(\lambda_i\sigma_i^{-1})/(\lambda_u\sigma_u^{-1})$ ratio controls the relative strength of smoothing constraints on the depth structure. Although the overall strength of regularization is tuned at each iteration, these ratios remain constant. We first set the $\sigma_i^{-1}/\sigma_u^{-1}$ as 0.02, which balances the average values of the normalized Fréchet derivatives for the two types of model parameters [*Hobro et al.*, 2003]. Besides, we set the $(\lambda_i\sigma_i^{-1})/(\lambda_u\sigma_u^{-1})$ as unity. After 18 iterations, the $\chi^2$ value was reduced to 0.85. The traveltimes of Pg and PmP arrivals were fitted well at all offsets (Figure 3). The resultant 3-D model is hereafter referred to as the standard solution. The crustal thickness and a cross section running over the segment center along the spreading direction Figure 4 from the resultant 3-D model (the standard solution) are shown in Figures 5e and 6e, respectively.

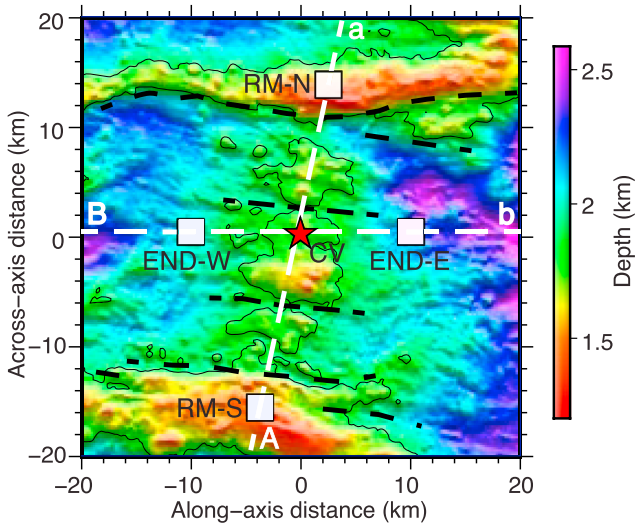


**Figure 4.** Bathymetry around the segment center. Its geographic location is shown in Figure 1b, with the same geological features. This $40 \times 40$ km$^2$ area represents the central part of the inverted model and has the best resolution. Line Aa marks the location of the vertical cross-section running over the segment center along the spreading direction, which is shown in Figures 6 and 8. Line Bb is the one running along the ridge axis, which is shown in Figures 8. The four white boxes show the $2.4 \times 2.4$ km$^2$ areas, within which the velocity-depth profiles are averaged and shown in Figure 9, whereas another box that coincides with the CV is not shown here. CV: central volcano (the segment center); END-W and END-E: 10 km away from the segment center toward the western and eastern segment ends; RM-S and RM-N: the southern and northern rift mountain.

To examine the effect of the velocity-depth trade-off, we modified the $\sigma_i^{-1}/\sigma_u^{-1}$ to 0.1 or 0.005 and altered the $(\lambda_i\sigma_i^{-1})/(\lambda_u\sigma_u^{-1})$ to 2 or 0.5. Figures 5 and 6 show seven different solutions with one or two regularization-strength weighting changes as compared to the standard solution. We also show another solution (Figures 5a and 6a), which was derived with the same regularization parameters as the standard solution, except using a layer stripping strategy that first updates the velocity structure to fit the Pg arrivals [*Zelt*, 1999]. All these resultant models fit the data with $\chi^2$ values between 0.8 and 0.9. Several common features can be seen in these solutions. First, the crustal thickness is almost constant along the spreading direction (Figures 5 and 6), whereas it quickly decreases away from the segment center along the ridge axis. Second, in all the solutions, the cross sections running through the segment center along the spreading directions clearly show low-velocity anomalies (LVA) beneath the ridge axis (Figure 6). However, differences exist in the detail of these features and in the small-scale fluctuations of the crustal thickness.

The solution derived with the layer stripping strategy (Figures 5a and 6a) shows great similarities to the standard solution. The change in the relative strength of the damping constraints also seems to have little effect on the result. This is reasonable, as the overall damping constraint ($\epsilon$ in equation (1)) was kept as small as possible if the inversion was stable. Besides, it was eventually removed when the $\chi^2$ reached 2, and eight more iterations were run to allow the model to jump to the smoothest solution [*Hobro et al.*, 2003; *Shaw and Orcutt*, 1985]. On the contrary, the relative strength of smoothing constraints plays an important role because it affects the definition of the smoothest model. In the models with less smoothing constraints on the depth structure, the crustal thickness has more fluctuations along the spreading direction with a wavelength of ~10 km (Figures 5d and 5g). The amplitude of the along-axis variation of the crustal thickness is also larger. The lower crustal LVA is of smaller size and amplitude (Figures 6d and 6g). The models with larger smoothing constraints on the interface depth structure show the opposite features (Figures 5 and 6) and contain visible differences in the velocities within the ~1 km thick layer immediately above the Moho interface. For example, the low-velocity body at 10 km across-axis distance around the Moho interface is of a much smaller size than the expected resolution (Figure A1) and disappears in other models, suggesting the artifacts arising from the uncertainty in the Moho depth.

From these tomographic models, the maximum crustal thickness beneath the ridge axis always lies at the segment center and varies by ≤0.4 km, whereas the minimum crustal thickness near the segment ends varies more (≤1 km) because there is less ray coverage (Figure 5 and Figure S1 in the supporting information).

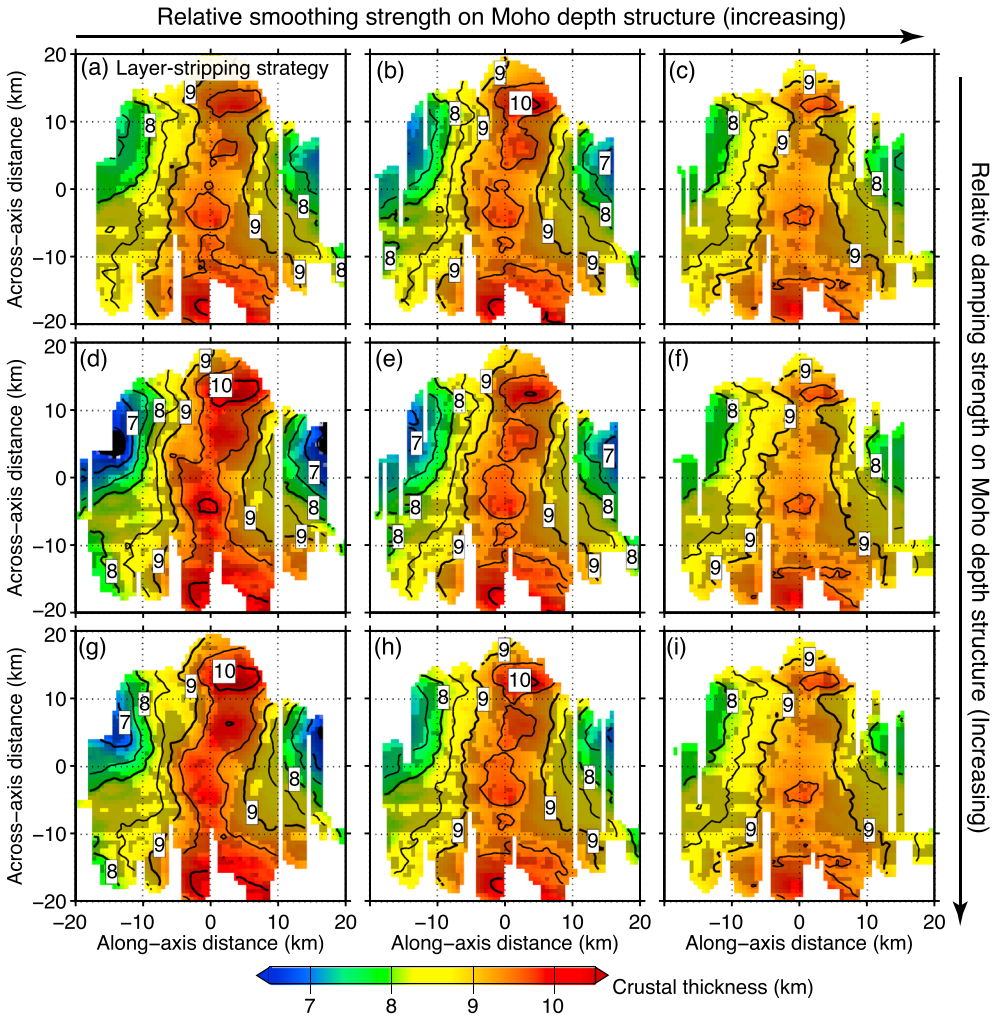


**Figure 5.** Comparison of the crustal thicknesses associated with the alternative solutions. The thickness values are represented by colors as well as contours, which are plotted at every 0.5 km and labeled at every 1 km. The color is shaded for the grid nodes without direct data constraints, but constrained by the across-axis smoothing that connects them to data-constrained grid nodes. Otherwise, the grid nodes beyond the data coverage are masked. (e) The standard solution, whereas the relative strength of the smoothing constraint on the depth structure is doubled for the right column and halved for the left column. The relative strength of the damping constraint on the depth structure is 5 times larger for the bottom row, and one quarter for the top row. An exception is (a), which was derived with the same regularization parameters as the standard solution (e), but with a layer stripping strategy. Note that the crustal thickness was calculated by subtracting the seafloor depth from the inverted Moho depth. The short-wavelength roughness is mostly inherited from the seafloor topography. See the text for more details.

The velocities generally vary by ≤0.02 km/s except in two places (Figure 6 and Figure S2). First, the ~1 km thick layer immediately above the Moho interface contains more variable velocities due to its strong trade-off with the short-wavelength fluctuations of the Moho depth, preventing effective interpretations. Second, the velocities at the center of the lower crustal LVA vary by ≤0.2 km/s. It is usually difficult to reveal LVA through the ray-based tomographic inversion, since the seismic energies penetrating its inside are strongly attenuated to form a shadow zone, which inhibits traveltime picking (Figure 2a). In addition, the finite-frequency effect through wavefront healing smears its effect on data [*Hung et al.*, 2000; *Xue et al.*, 2015]. While the location of the LVA is well constrained by the ray path surrounding it, the recovered amplitude is of larger uncertainty and usually under-estimated.

In summary, the trade-off has very small effect on the long-wavelength features (> ~10 km) of the lower crustal velocity and the Moho depth. This may be attributed to the fact that the near-critical PmP reflections have been picked over a wide range of source-receiver offsets (e.g., ~31–52 km, Figure 2a). However, the

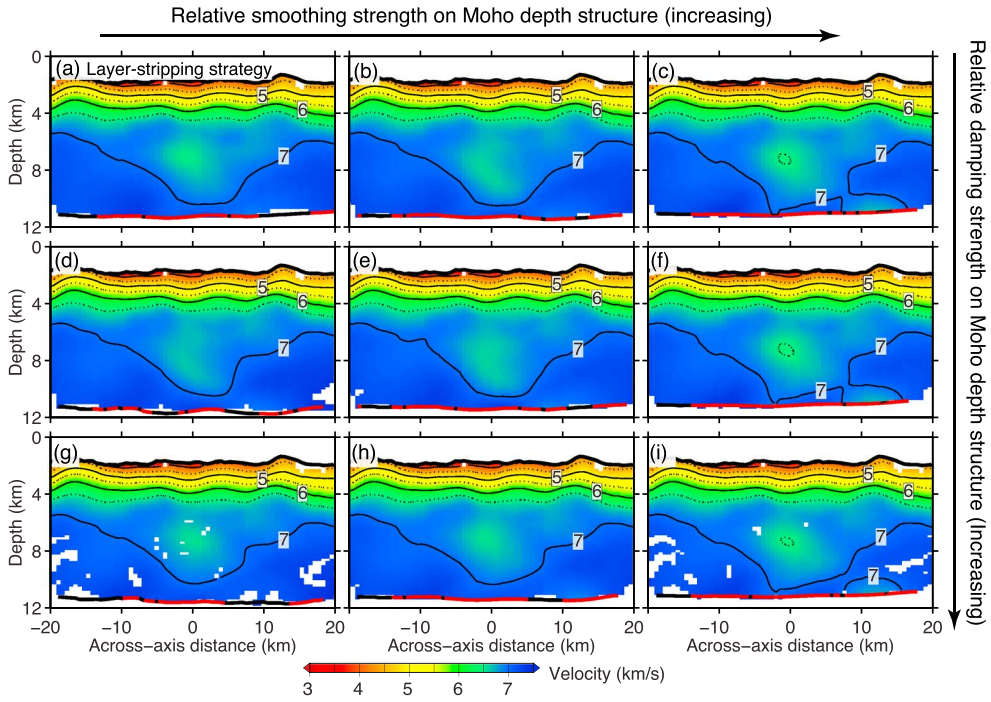


**Figure 6.** Comparison of the velocities associated with the alternative solutions. The location of these cross sections is shown in Figure 4 as line Aa. The velocities are contoured at every 0.5 km/s with labels at every 1 km/s. The seafloor and Moho interface bound the crust at its top and bottom, respectively. The red color along the Moho interface indicates the PmP reflection points. Velocity nodes without ray coverage are masked, and the arrangement of the models is the same as in Figure 5. See the text for more details.

quantitative aspects of the long-wavelength variations are apparently affected, as well as the short-wavelength variations. In the following sections, we use the standard resolution (Figures 5e and 6e) as an example for interpretation, but we only interpret the features that are common in all the alternative solutions.

### 4.3. Crustal Thickness

The Moho interface was smoothed in terms of depth below sea level (bsl), instead of below seafloor (bsf). The crustal thickness shown in Figure 5 would inherit lateral variations from the seafloor topography, especially at the short wavelengths. For comparison, the Moho topography is also presented in the 2-D cross sections (Figure 8). The data constraint on the Moho depth structure is directly reflected by the distribution of PmP reflecting points. In Figure 5, the crustal thickness constrained by the PmP reflecting points is shown with bright colors. Good data coverage can be seen at the segment center and toward the western end, and it continues to ±15–20 km across-axis distance. In contrast, the data coverage is much poorer toward the eastern segment end (at along-axis distance >5 km) with only scattered reflecting points. Therefore, no detailed variations should be interpreted at that part.

For the first-order variations, the crustal thickness around the segment center is almost constant along the spreading direction and thins toward the segment ends. These are the common features in all the alternative models (Figure 5). Beneath the ridge axis, the maximum crustal thickness lies at the segment center and varies between ~9.3 km and ~9.8 km in the different models, whereas the minimum crustal thickness near the segment ends varies between ~6.6 km and ~7.6 km. The seafloor bathymetry could account for 20%–35% of the along-axis variation of the crustal thickness, while the rest of the variation arises from the Moho topography (e.g., Figure 8b). Second-order variations with wavelengths about 10 km and shorter-wavelength fluctuations of the crustal thickness can be seen along the spreading direction. However, they are significantly attributed to the bathymetry or the poor data constraint near the edge of the model and less stable in the alternative solutions. Hence, we will focus on the first-order variations in the interpretations.

*Li et al.* [2015] further analyzed a long profile along the ridge axis including segment 27 and extending beyond the NTD on the west, by using our result as a part of input to a 2-D first-arrival traveltime tomography. They found mantle velocities (>7.3 km/s) at ~4 km below the NTD basin at ~40 km away from the segment center.

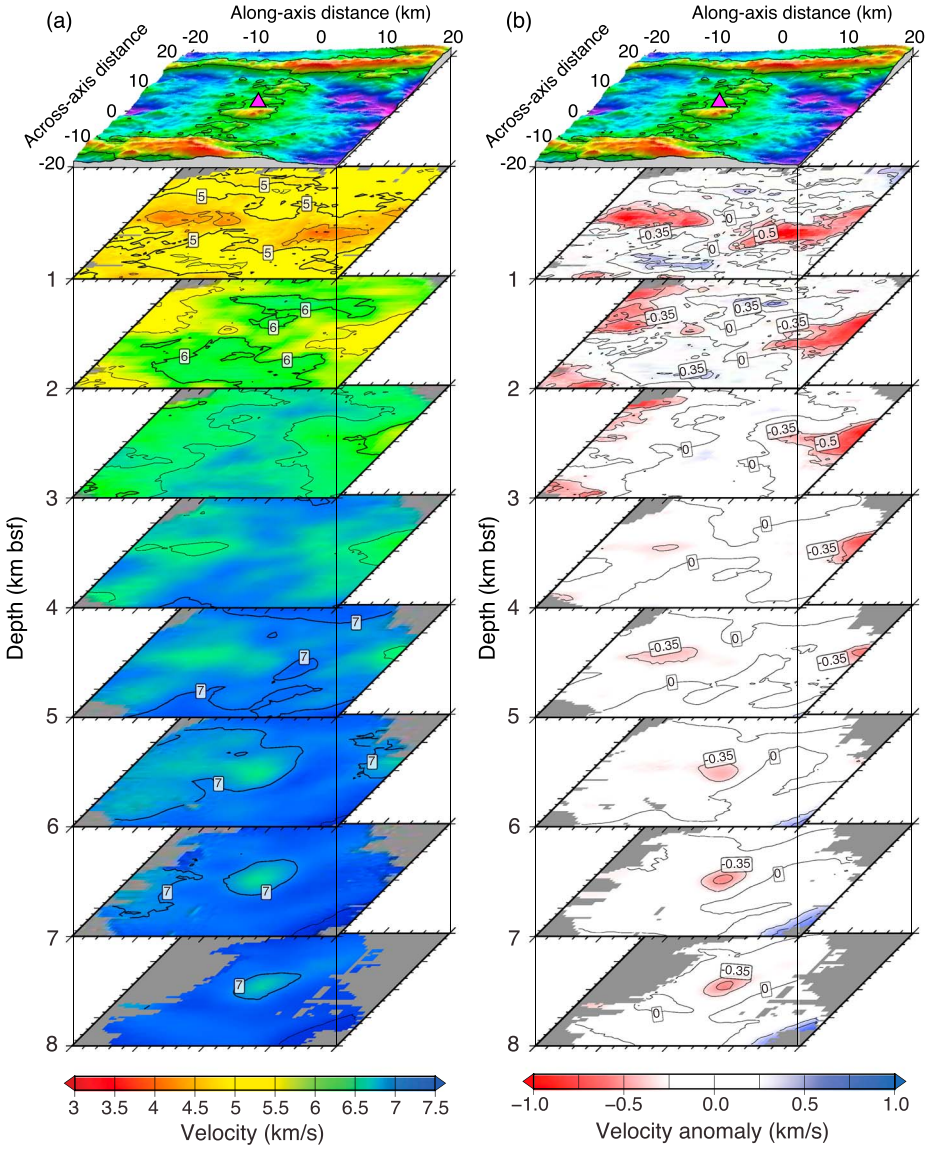


**Figure 7.** Lateral variations of the 3-D crustal model from the standard solution at 1–8 km depth bsf, capped by the seafloor topography for (a) velocities and (b) velocity anomalies. The anomaly is calculated with respect to the average velocity-depth profile shown in Figure 9. Model nodes with no ray coverage are masked. The velocities are contoured at every 0.5 km/s and labeled at every 1 km/s. The anomalies are contoured at 0, ±0.35, and ±0.5 km/s.

*Niu et al.* [2015] also analyzed the same profile by incorporating the PmP arrivals in the tomographic inversion. They also confirmed the pattern of the along-axis variation of crustal thickness, whereas the maximum crustal thickness that they found is ~10.2 km beneath the segment center. The slightly larger value may be due to the absence of the lower crustal LVA in their model, which is unlikely to be revealed without the across-axis data.

### 4.4. Three-Dimensional Velocity Structure

While the regularization controls the quality of the accepted models, the ray coverage determines the resolution limit. We performed checkerboard tests to assess the resolvability on the 3-D velocity model (Appendix A). These tests indicate a generally good resolution within the central 40 × 40 km$^2$ area. Checkerboard anomalies with half wavelengths larger than ~4×1 km$^2$ can be recovered at the depth above 8 km below sea level (bsl). Below that, checkerboard anomalies with half wavelengths larger than ~8.5×1.9 km$^2$ can be recovered. Figure 7 shows the horizontal slices of the velocities and anomalies from the standard solution at every 1 km depth below seafloor (bsf). The anomalies are calculated with respect to the average of the data-constrained velocities within ±15 km along-axis distance at each depth bsf. The average velocity-depth profile is shown

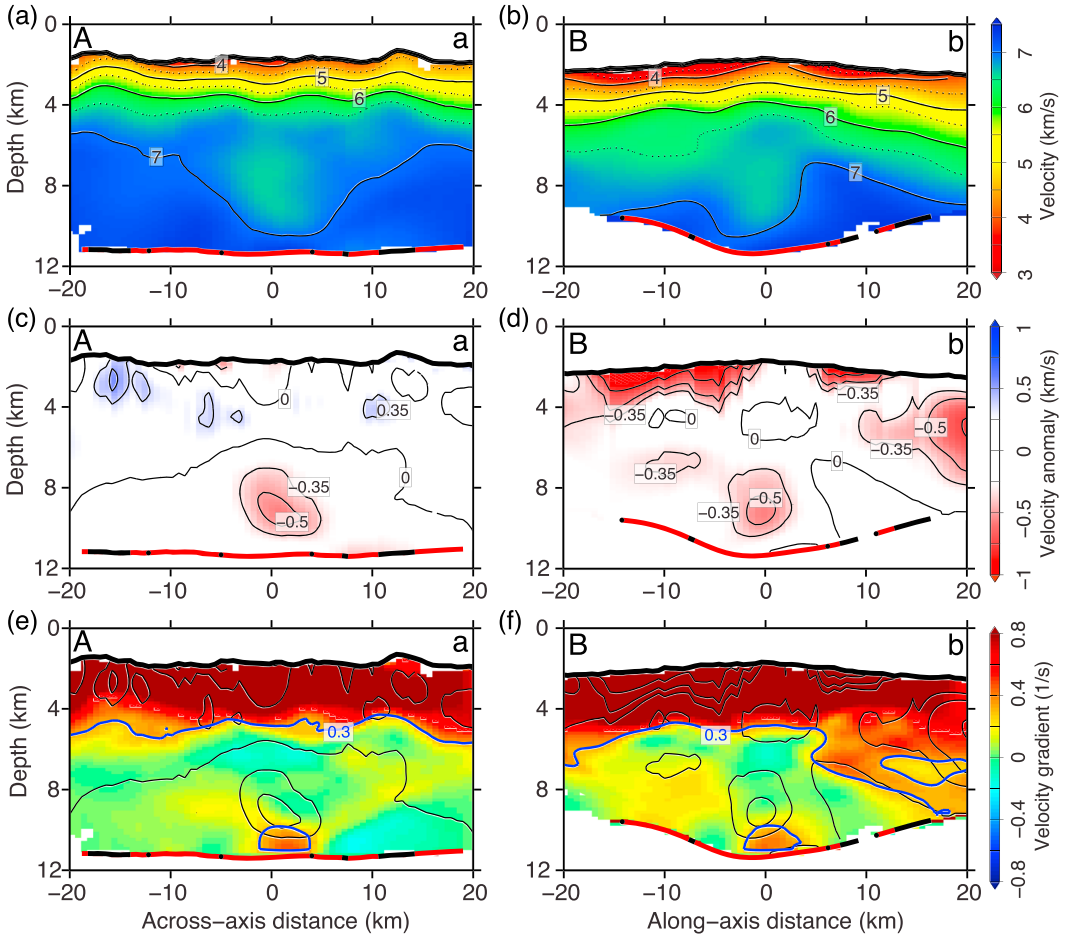


**Figure 8.** Cross sections from the standard solution, shown as (a, b) velocities, (c, d) velocity anomalies, and (e, f) vertical velocity gradients. The left and right columns are for the profiles running over the segment center along the spreading direction (line Aa in Figure 4), and along the ridge axis (line Bb in Figure 4), respectively. The velocities are contoured at every 0.5 km/s and labeled at every 1 km/s. The anomalies are contoured at 0, ±0.35, and ±0.5 km/s. The gradients are contoured at 0.3 $s^{-1}$ with blue curves, whereas the black curves in Figures 8e and 8f repeat the contours of anomalies for comparison. The Moho interfaces at the bottom of the model are shown as thick curves, in which the red color marks the PmP reflection points.

in Figure 9. Figure 8 shows two vertical cross sections running over the segment center along the spreading direction and along the ridge axis, respectively. Besides the velocity, the anomalies and the vertical velocity gradients are also calculated and shown along these cross sections. Figure 9 extracts 1-D velocity-depth profiles at five distinct regions, whose locations are marked in Figure 4.

In the upper crust (< ~3 km bsf), an hourglass-shaped LVA lies around the axial zone, with the weakest anomaly at the segment center (Figure 7b). On the west side of the segment center, it continues to a depth less than 3 km bsf, whereas on the east side it extends to 4–5 km bsf. This difference can also be seen in the vertical velocity gradient plot, where high gradients extend deeper on the east side (Figure 8f). Across the segment center, the velocity contours in the upper crust closely follow the seafloor topography along the spreading direction (Figure 8a). The vertical gradient also shows a relatively uniform upper crustal layer (Figure 8e). A few scattered high-velocity anomalies are occasionally observed off the ridge axis (Figure 8c).

In the lower crust (>4 km bsf), the most significant feature is the lower crustal LVA beneath the segment center, which has been present in all the solution models (Figure 6). The accurate size of the LVA is difficult to be identified due to the smearing within the Fresnel zone. As a proxy, we measure the dimension of the contour of −0.35 km/s, which is laterally rounded with a diameter of 7–8 km at 7 km depth bsf. The depth variation of the anomaly is additionally affected by the average velocity-depth variation and has higher uncertainties. However, the negative vertical gradient in the velocity-depth profile beneath the segment center suggests

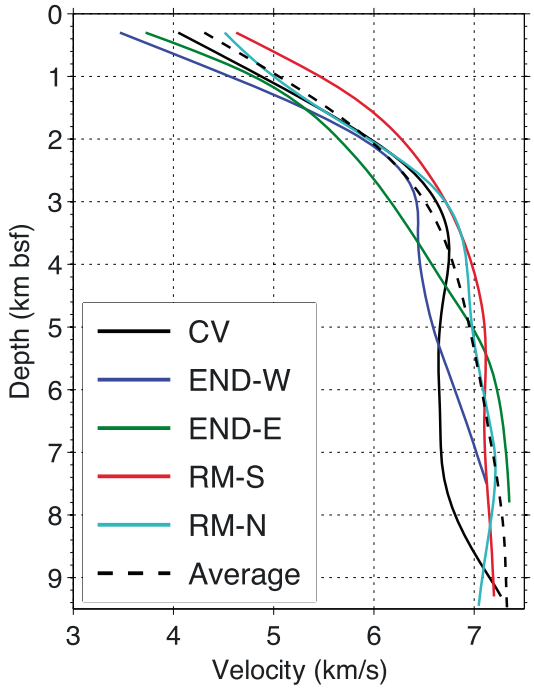


**Figure 9.** Velocity variations along depth. The black dashed curve is the average of the data-constrained velocities within the along-axis distance of ±15 km. The five solid curves represent the velocity-depth variations at five different locations, as shown in Figure 4. Each of them is an average within the corresponding $2.4 \times 2.4$ km$^2$ area. Velocities above 0.3 km bsf are masked due to the poor constraints at that depth of the OBS data set.

that the LVA starts at ~4 km bsf (Figure 9). Its bottom is close to the Moho interface, whereas the interaction between them may be poorly resolved due to the velocity-depth trade-off. The maximum anomaly is ~ −0.6 km/s compared to the 1-D average model in the standard solution model. Nonetheless, it is possible that this anomaly corresponds to a narrower LVA with larger amplitude in the true earth model, which has been smoothed by the tomography.

At the midcrustal depth (4–5 km bsf), a small axial LVA is observed on the west side of the segment center, which is centered at −8 km along-axis distance and at about 7 km depth bsl (Figure 8d); here the model resolution is good enough to constrain this LVA. Its maximum amplitude is about −0.4 km/s, lying at 5 km bsf (Figure 7b). Its lateral extension (sampled by the −0.35 km/s contour) along the ridge axis (~8 km) is about double that across the ridge axis (~4 km). Also importantly, this small LVA is separated from the overlying upper crustal LVA by a small high-velocity body.

The 1-D velocity-depth profiles beneath the northern and southern rift mountains show great similarity, both having large velocity gradients and decreased velocities in the upper crust and small gradients in the lower crust (Figure 9). No velocities exceed 7.3 km/s. The velocity beneath the segment center also has this pattern, except having negative gradients at the top of the lower crust. While the 1-D profile near the western segment end still exhibits the two-layer pattern, the one near the eastern end shows significant velocity gradients in the whole crust. This difference is also reflected by the seismic data sampling the two distinct types of lower crusts. Within the segment center, the Pg refractions are rapidly attenuated at long offsets, and the critical-angle PmP reflections are observed at relatively shorter offsets because more seismic energies traverse the low-gradient lower crust with higher angles and reflect off the Moho interface (Figures 2a and 2c). Otherwise, without the low gradients, the Pg refractions are quite strong at long offsets, and the critical-angle PmP reflections are not observed (Figure 2d). This may also explain why the PmP reflection points are largely absent on the east side of the segment center (Figure 5).

### 4.5. Azimuthal Anisotropy

As the inversion approach tries to minimize the overall misfit in a least squares sense, there could be some systematic distributions of the residuals that are not explained by the inverted model. Particularly, the distribution of residuals with respect to the ray azimuth may be indicative of anisotropy that is not included in

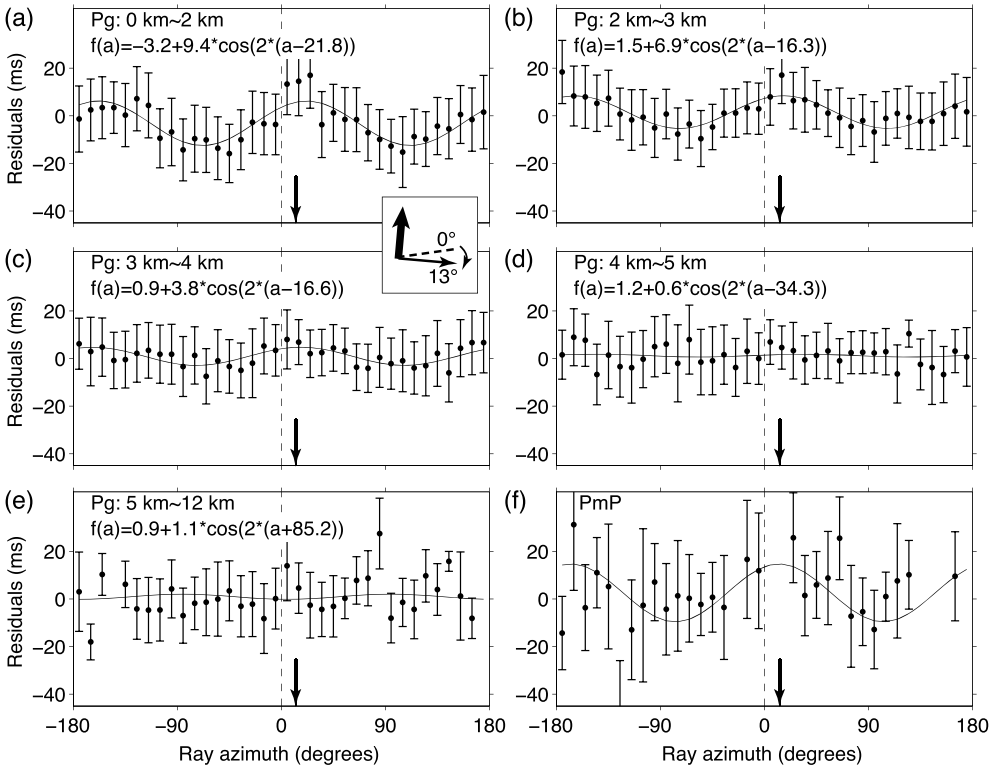


**Figure 10.** Mean traveltime residuals of all instruments for (a–e) Pg arrivals and (f) PmP arrivals. The Pg residuals were first binned according to their turning depth below the seafloor. Then, within each turning depth window (marked in the corner of each panel), the residuals were binned every 10° of the source-receiver azimuth. The average values are shown as dots with the width of error bars indicating a standard deviation. The solid line is the best fitting cosine curve corresponding to the formula shown in the corner. The inset in Figures 10a and 10c illustrates the polar coordinate system, where the azimuth angle of 0° is parallel to the ridge axis trend (dashed lines in all the panels). The thin solid arrows in all the panels mark the direction perpendicular to the spreading direction (shown as the thick arrow in the inset), 13° clockwise from the ridge axis trend. A positive residual means that the predicted traveltime is larger than the observed, so the fast direction of wave propagation corresponds to the peak of the curve, whose azimuth can be easily read from the formula.

the isotropic velocity model. Previous 3-D traveltime tomography studies at faster spreading segments have consistently shown a cos(2*a*) (*a* represents the ray azimuth) pattern of the azimuthal distribution of residuals [e.g., *Seher et al.*, 2010a; *Dunn et al.*, 2005; *Barclay et al.*, 1998; *Weekly et al.*, 2014].

Figure 10 shows the azimuthal distribution of the mean residuals associated with the turning depths. These residuals were computed from the standard solution. They were fitted with cosine curves, and the fitting is good for Pg residuals. The peak-to-peak variation of the best fitting curve is ~19 ms for the Pg ray paths turning above 2 km bsf. It gradually decreases to ~14 ms at 2–3 km bsf and ~8 ms at 3–4 km bsf and disappears below 4 km bsf. Although the best fitting curve for PmP residuals exhibits a large amplitude, the data fitting is too poor to support a meaningful conclusion. This pattern would require an azimuthal anisotropy of about 1%–2% within the top 2 km bsf, decreasing to <0.2% below 3–4 km bsf, assuming a 1-D isotropic velocity structure as the average model shown in Figure 9. The anisotropy has a fast direction oriented 16°–22° clockwise from the ridge axis trend, close to the spreading-normal direction (Figure 10, inset).

Since the anisotropy is extracted from the residuals of an isotropic inversion, it can only be recovered in the areas with even ray azimuth coverage. Otherwise, it would be mapped into the isotropic velocities as heterogeneities, whose amplitude might be too small to be detected as obvious anomalies. In this study, the anisotropy estimation is valid around the center of the model.

## 5. Interpretation

We have presented the 3-D crustal seismic image of the ultraslow-spreading ridge segment with excess melt supply [*Li et al.*, 2015; *Sauter et al.*, 2009]. It is significantly different from previous seismic images at the

ultraslow-spreading ridge segments [e.g., *Minshull et al.*, 2006; *Jokat and Schmidt-Aursch*, 2007; *Jokat et al.*, 2012], which found much thinner crusts as compared to the global average of 6 km [*Chen*, 1992; *Bown and White*, 1994] and the lack of the lower crustal velocities (between 6.5 km/s and 7.2 km/s). *Li et al.* [2015] has demonstrated that the thick crust at the segment center rapidly decreases toward the segment ends, suggesting an enhanced focusing mechanism of the melt supply to the segment center from the mantle. Here we interpret the inverted 3-D crustal velocities in terms of the interplay of the tectonic and magmatic accretions under the ultraslow-spreading environment.

### 5.1. Upper Crust

Extensive seismic observations at fast- and slow-spreading ridges have demonstrated that the upper crust is characterized by high vertical velocity gradients (>1 $s^{-1}$), low velocities (<6.5 km/s), and anisotropy [e.g., *Harding et al.*, 1993; *Canales et al.*, 2000b; *Hosford et al.*, 2001; *Dunn et al.*, 2005; *Seher et al.*, 2010a, 2010b]. This layer is named layer 2 and composed of extrusive basalts and dykes [*Detrick et al.*, 1994]. It is cool and brittle as indicated by the prevalence of microearthquakes [*Barclay et al.*, 2001; *Crawford et al.*, 2013; *Weekly et al.*, 2013] and supported by the thermodynamic modeling [*Morgan and Chen*, 1993]. The seismic velocity variation in this layer is closely related to porosity [*Berryman et al.*, 2002]. At the slow-/ultraslow-spreading segments, the porosity is mainly influenced by the tectonic extension that fractures and cracks the brittle layer downward from the seafloor, which can be filled or closed by the residue of hydrothermal circulation and increasing pressure. For example, the general increase of velocity with depth corresponds to the closure of pore space with increasing confining pressure and temperatures (Figure 9). Additionally, the widely observed anisotropy suggests that these cracks are vertically oriented and aligned by the local stress field [*Barclay et al.*, 1998].

By subtracting the average velocity-depth profile, we observe the lateral variation of the velocity anomalies (Figure 7). Above 2–3 km bsf, strong LVA lies around the ridge axis, indicating the region under active extension. It disappears in the aged crust away from the ridge axis. This is usually explained by the hydrothermal deposition that fills the pore space [*Dunn et al.*, 2005; *Carlson*, 1998]. Other factors related to the axial low velocities near the seafloor may include porous extrusive [*Dunn et al.*, 2005] and hot rocks or retained magma related to recent magmatic activities [*Barclay et al.*, 1998; *Magde et al.*, 2000]. However, the presence of hot rocks or retained magma is clearly inconsistent with the presence of anisotropy that suggests a cold and cracked upper crust. The porous extrusive should correspond to volcanic edifices and hydrothermal activities [e.g., *Arnulf et al.*, 2011]. Nonetheless, at the central volcano of this study segment, the LVA is much weaker. Hence, the shallow axial LVA should be mostly attributed to the active extension. The relatively high upper crustal velocities beneath the volcano may be due to magmatic intrusions that fill the tectonic voids. Even higher-velocity bodies that are discretely distributed along the flow line may represent the cooled dykes created during more magmatically robust periods or emplacement of deeper crust at shallower depth by faults [*Seher et al.*, 2010a].

The bottom of the fractured layer 2 is usually defined by the velocity of ~6.5 km/s, whereas the vertical velocity gradients (Figures 8e and 8f) can provide additional constraints on the depth of the fracturing front. For the crust formed around the segment center, the velocity rapidly increases to 6.5 km/s at ~2.5 km bsf due to the closure of pore spaces. The gradients decrease to <0.3 $s^{-1}$ until 3–3.5 km bsf, below which the gradients remain small and less variable, suggesting that the closure of pore space is not complete until that depth. *Detrick et al.* [1994] have observed sheeted dykes that below the depth of 6.5 km/s contour in a drill hole. Thus, dyke injections into fractures are possible at depths with velocities >6.5 km/s, and the velocity gradients may provide more reasonable constraints on the bottom of layer 2. The observation of anisotropy at 3–4 km bsf (Figure 10c) is also consistent with this conclusion. Within the cross section along the spreading direction, both the velocity contour of 6.5 km/s and gradient contour of 0.3 $s^{-1}$ closely follow the seafloor topography and define a highly constant layer 2 thickness since 3 Ma (Figures 8a and 8e). On the west side of the segment center, the velocity contour is slightly perturbed whereas the gradient contour suggests that the layer 2 thickness is almost constant. However, on the east side, both contours indicate a much thicker layer 2, which will be discussed below.

The anisotropy observed here is smaller than that observed at the slow-spreading OH-1 and Lucky Strike segments [*Seher et al.*, 2010a; *Dunn et al.*, 2005]. Despite the large uncertainty of this estimation, it may be combined with the elevated upper crustal velocities at the segment center to suggest that the dyke intrusions are more frequent in the unit of per increment, due to the slower spreading rate and/or more melt supply. The frequent intrusions may also be responsible for the construction of the relatively continuous topography along the spreading direction across the segment center.

The fast direction of the anisotropy seems to be constant at all depths (N98–114°E) and is closer to the spreading-normal direction (~N95°E), rather than the segment-scale ridge trend (~N82°E). The local trend of the ridge axis and fabrics around the segment center also strike subperpendicularly to the spreading direction. It has been suggested that under the oblique-spreading environment, the axial rift valley acts as a weakness zone to localize the brittle failures, whereas the trend of intrarift fabrics are mainly controlled by the orthogonal extension or transtension [*Sauter et al.*, 2002; *Cannat et al.*, 2008; *Dick et al.*, 2003; *Tuckwell et al.*, 1998]. Side-scan sonar images at other oblique-spreading ultraslow ridge segments have revealed the systematic variation from magmatic segment centers to segment ends, where faults become more oblique, shorter, and denser [*Sauter et al.*, 2002; *Curewitz et al.*, 2010]. Our results demonstrate that the orthogonal extension and dyke injection are favored throughout the lithosphere at the magmatic segment center, possibly due to the small thickness of the lithosphere and the magma pressure from the asthenosphere.

### 5.2. Mid to Lower Crust

The velocities are constrained down to the Moho depth in the central $40 \times 40$ km$^2$ area of the model. The fact that no velocity exceeds 7.3 km/s suggests that the lower crust is composed of gabbros [*Canales et al.*, 2000a]. Nonetheless, for the thin crust at ultraslow-spreading ridges, it has been proposed that the seismic Moho may correspond to an alteration front separating the partially serpentinized mantle and the normal mantle [*Muller et al.*, 1997], where the serpentinite takes a velocity comparable to dykes and gabbros. If the serpentinization is extant down to the Moho depth, the whole crust should be fractured and porous to allow deep penetration of seawater, which would exhibit high velocity gradients from the seafloor down to the Moho [e.g., *Muller et al.*, 1997; *Canales et al.*, 2000a]. However, our results clearly show the typical igneous crustal structure at most parts, with a high-gradient layer 2 overlying a low-gradient layer 3. More importantly, the Moho is observed at $> \sim 7$ km bsf, where the temperature would be too high to maintain stable serpentinites [*Bonatti et al.*, 1984; *Minshull et al.*, 1998]. We thus suggest that the serpentinite is less likely to be present in the lower crust in our study area.

Three groups of low-velocity anomalies are present in the mid to lower crust (≥3–4 km bsf) beneath the ridge axis: (a) at the segment center, (b) toward the eastern segment end, and (c) toward the western segment end. We will interpret them separately in this section.

#### 5.2.1. Low-Velocity Anomalies at the Segment Center: Evidence for Partial Melt

The LVA at the segment center starts at 4–5 km bsf and extends down to the Moho depth. Similar structures have been imaged at the slow-spreading MAR segment centers, such as at the OH-1 segment [*Dunn et al.*, 2005] and the Lucky Strike segment [*Seher et al.*, 2010a]. The coexistence of shallow volcanoes and hydrothermal activity at the seafloor suggests that elevated temperatures and/or small amounts of melt should be responsible for the LVA. The discovery of a melt lens reflector atop the lower crustal LVA at the Lucky Strike segment strongly supports that the LVA corresponds to a crustal magma system [*Singh et al.*, 2006].

Considering the coincidence with the thick crust, *Li et al.* [2015] has also interpreted the lower crustal LVA at this segment center as a crustal magma chamber. The maximum anomaly is $\sim -0.6$ km/s compared to the off-axis velocity that was formed at the segment center and is cooled now (Figure 9). If the temperature is the only reason, an anomaly of ~1000° is required (assuming $\delta log V_P / \delta t = -8.1 \times 10^{-5} K^{-1}$ [*Christensen*, 1979]). This value may become smaller if we consider the importance of anelasticity at very high temperatures [*Dunn et al.*, 2000; *Karato*, 1993]. However, due to the large depth of the anomaly and thus a high off-axis background temperature, it is very likely that the lower crustal temperature at the segment center (the temperature anomaly plus the off-axis background temperature) exceeds the solidus (~1200°), and therefore, a small amount of melt is required.

#### 5.2.2. Low-Velocity Anomalies Toward the Western Segment End: Evidence for Magma Redistribution

The small low-velocity anomaly extending toward the western segment end is mostly confined within 3.5–6 km bsf. Its maximum amplitude is about −0.4 km/s, lying at 5 km bsf, where it approaches a maximum distance of more than 15 km away from the segment center. The velocity-depth profile cutting into the anomaly shows a slightly negative gradient at its top (profile END-W, Figure 9), which separates it from the overlying low velocities in layer 2. Thus, we exclude the contribution of an increased porosity due to the fracturing initiated from the seafloor, because the breaking of the high gradient indicates almost complete closure of pore spaces above the anomaly.

We ascribe this midcrustal LVA to elevated temperatures, whereas melt is not required by our results or its amount is too small to be detected. It could be heated by the hot materials redistributed from the

segment center, most likely through lateral dyke injections as observed at different volcanic sites [e.g., *Dziak et al.*, 1995; *Ryan et al.*, 1981]. To further identify such dyke injection events at this study segment, microearthquake studies would be required.

#### 5.2.3. Low-Velocity Anomalies Toward the Eastern Segment End: Evidence for Deep-Penetrating Fractures

Toward the eastern segment end, the low velocities extend from the seafloor down to a much larger depth than at the segment center. More importantly, the distinct change in velocity gradients that characterizes the oceanic layer 2/3 boundary also takes place at large depths (e.g., 5.5 km bsf at the profile END-E, Figure 9) and eventually reaches the Moho depth at the eastern end of the model (Figure 8f). The constant-gradient layer is similar to the observations at discontinuities of slow-spreading ridges [*Canales et al.*, 2000a; *Detrick et al.*, 1993] and within the thin crusts at ultraslow-spreading ridges [*Jokat et al.*, 2012; *Minshull et al.*, 2006]. Beneath the western NTD basin, *Li et al.* [2015] also show a constant-gradient feature. The favorable interpretation at those locations is an intensely fractured and altered basaltic layer overlying partially serpentinized mantle [*Canales et al.*, 2000a].

As we have suggested above, the LVA at the center of the segment is associated with the presence of elevated temperatures and melt. Although this anomaly is localized, its influence would extend far from the center, and hence, serpentinite is unlikely to be present in its vicinity. Therefore, we attribute the deep-penetrating, constant-gradient low velocities to high porosities caused by intense fracturing within the igneous crust. Toward the eastern segment end, the fractured layer gradually thickens and the underlying unfractured gabbroic layer is pinched out, indicating a more important role of the tectonic component in the crustal accretion process.

## 6. Discussion

### 6.1. Comparison With Other Spreading Segments

The most significant difference as compared to previously studied ultraslow-spreading segments [e.g., *Jokat et al.*, 2012; *Minshull et al.*, 2006; *Zhao et al.*, 2013] is the presence of a much thicker crust and the crustal magma system, both indicating an excess melt supply to this segment that has been persistent for more than 3 Ma [*Li et al.*, 2015]. In addition, the maximum crustal thickness beneath the segment center (~9.5 km) is even larger than those at the slow-spreading MAR segments that also contain similar lower crustal magma chambers [*Seher et al.*, 2010a; *Dunn et al.*, 2005]. Excessively thick crusts are generally associated with mantle heterogeneities. For example, the ridges around Iceland have been reported to overlie very thick crusts (tens of kilometers) [*Artemieva and Thybo*, 2013], which are clearly due to the extra melt supply from the hot mantle plume. The maximum crustal thickness at the Lau spreading center is also observed >9 km [*Arai and Dunn*, 2014], whereas observations in various aspects agree that significant contributions come from a hydrous mantle source above the subducting Pacific plate [*Eason and Dunn*, 2015]. At our study area, *Li et al.* [2015] argued that none of these mantle heterogeneities are large enough. Instead, the focusing mechanism of the mantle upwelling may be enhanced by the large slope of the lithosphere-asthenosphere boundary beneath the ultraslow-spreading ridge and is responsible for the formation of the thick crust.

The thickness of layer 2 that we have observed is 3–3.5 km at the segment center and on its west side, comparable to that at slow-spreading segments [*Seher et al.*, 2010a; *Dunn*, 2015]. The bottom of layer 2 at MOR seems well correlated to the brittle-ductile boundary [*Barclay et al.*, 2001], and systematically deepens from fast- to slow-spreading ridges, while the depth to the lower crustal magma chambers also increases [*Morgan and Chen*, 1993]. However, at the ultraslow-spreading ridges, the thickness of layer 2 varies significantly. For instance, *Jokat et al.* [2012] studied a 120 km long section of the Knipovich Ridge at 76°26′N and found an almost uniform layer 2 thickness of ~4.5 km that is emplaced over a serpentinized mantle directly. This is consistent with a relatively cold environment. On the other hand, *Minshull et al.* [2006] observed a 1.5–2.5 km thick layer 2 overlying a 0.5–3 km thick layer 3 at the SWIR at 66°E and attributed the thinner layer 2 (<2 km) to the exhumation of deeper crustal materials.

Although the thick crust indicates that our study segment is more magmatically robust and hotter than the SWIR segments at 66°E, the fractured layer 2 is obviously thicker at this segment center and even more toward the eastern segment end. We suggest that a combination of tectonic and thermally driven fracturing may explain this diversity. While the tectonic fracturing has maximum effects near the seafloor, the thermally driven fracturing should be strongest around the magma body. *Dunn* [2015] used similar mechanisms to explain the increased amplitude of anisotropy in the upper crust at more magmatically robust segments of

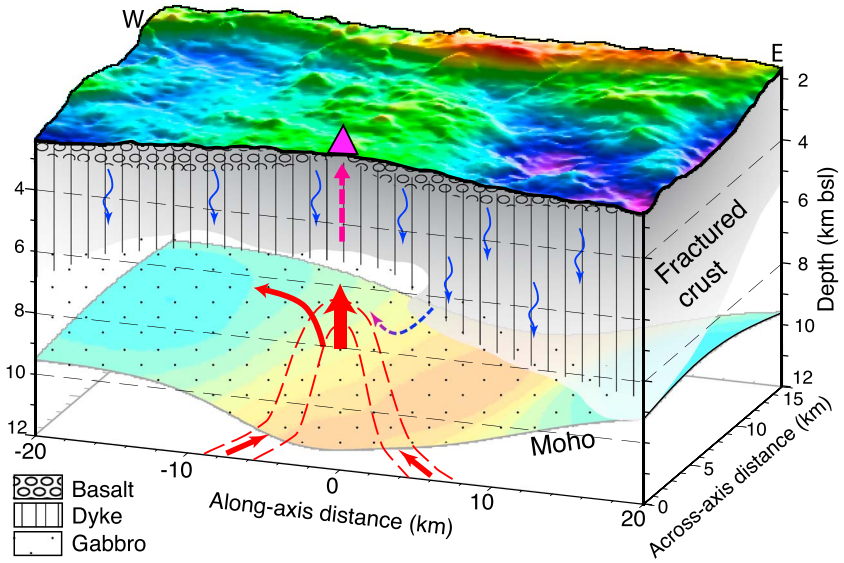


**Figure 11.** A schematic diagram illuminating the main features in the 3-D tomography results. The 3-D box represents the crust capped by the seafloor. On the bottom is the color-coded Moho interface. The crust is cut along the ridge-parallel profile Bb (Figure 4) at the front, where we mark the petrological structure based on the velocities. The red dashed curves are isothermals outlining the magmatic system below the segment center, as inferred from the lower crustal LVA. The red arrows describe the melt flow, which is focused to the segment center in the mantle, and then can be vertically injected to the upper crust or laterally redistributed at the midcrust along the ridge axis toward the western segment end. The grey areas are the intensely fractured crust as inferred from the vertical velocity gradients, which is potentially permeable. The magenta arrow shows a potential discharging flow of hydrothermal fluids below the extinct vent (magenta triangle). The blue curved arrows indicate the pervasive flows of cold sea water beneath the axial zone, which may reach a large depth on the east side of the magma body and cool the midcrust.

the East Lau spreading center. He suggested that the hydrofracturing combined with other processes like thermal contraction and fluid overpressure, could increase the tensile stress and porosity above the magma body. If this is true, we could expect a larger porosity at the lower part of the brittle layer here than that at 66°E, because *Minshull et al.* [2006] might have captured a snapshot of the crust when the compressive stress was not reduced sufficiently by the tectonic extension for the bottom of the brittle layer to break.

### 6.2. Implications for the Magmatic Accretion and Its Link to the Discontinuities

The 3-D seismic image gives insights into the details of crustal accretion at the ultraslow-spreading segment. Figure 11 shows a schematic diagram integrating the main results. The focused melt supply from the mantle enters the lower crust beneath the segment center and then can be injected vertically into the upper crust or laterally redistributed along the ridge axis at the midcrustal depth. The vertically injected dykes build the high-topography central volcano. The magma system may also have supported the extinct hydrothermal vent

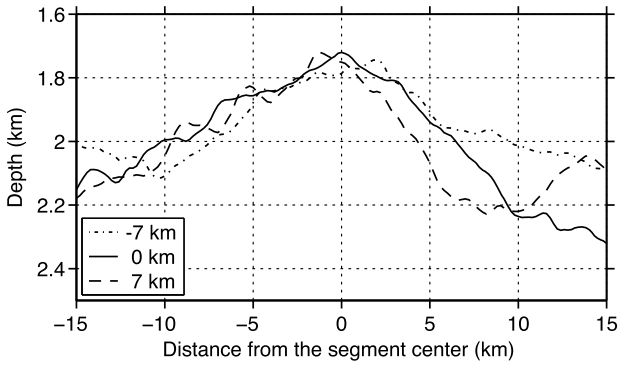


**Figure 12.** Bathymetric variations toward segment ends. The bathymetry profiles were extracted along the ridge trend at different distances to the current ridge axis (i.e., at different crustal ages) and then aligned according to the instantaneous locations of the segment center (line Aa in Figure 4). The depth profiles shown here are averaged within three 3 km wide bands that are centered at −7, 0, and 7 km distance away from the ridge axis.

[*Tao et al.*, 2012]. Although we cannot rule out that small melt bodies may enter the crust away from the segment center, it is clear that the magmatic construction is at its maximum at the segment center. On the other hand, the tectonic stretching is continuous along the ridge axis and dominates at the segment ends. So far, the scenario shares great similarities with that at the slow-spreading ridge segments [*Hooft et al.*, 2000; *Seher et al.*, 2010a].

However, as the slow-spreading ridges are significantly different from the fast-spreading ridges, the ultraslow-spreading ridges are also very distinct from them in terms of segmentation [*Dick et al.*, 2003; *Carbotte et al.*, 2015; *Sauter and Cannat*, 2010]. The magmatic segment centers at ultraslow ridges are usually narrower than the slow-spreading ridges, and a large portion of them are separated by long stretches of oblique-spreading and deep NTD domains. In some cases, the NTDs are too long for their midpoints to receive any significant melt either from the mantle or through the crustal-level redistribution from magmatic segment centers, forming a novel type of amagmatic spreading [*Cannat et al.*, 2008; *Dick et al.*, 2003]. The effect of the spreading obliquity on the mantle melting regime is less clear, but unlikely to be significant [*Li et al.*, 2015; *Cannat et al.*, 2008]. On the other hand, its effect on the crustal-level processes should be expected [*Cannat et al.*, 2008].

The segment 27 is bounded by two NTDs on the west and east sides. The eastern NTD has a much larger spreading obliquity than the western NTD [*Sauter et al.*, 2001]. Correspondingly, an asymmetry of the crustal structure is observed with respect to the segment center. Toward the western segment end, lateral dyke injection occurs at the top of layer 3 and may be controlled by the rheological contrast across the brittle-ductile boundary [*Hooft et al.*, 2000]. Toward the eastern segment end, the fracturing front starts to deepen at 5 km away from the segment center and finally approaches the Moho depth at 20 km along-axis distance, suggesting much colder crustal temperatures. The asymmetry of the thermal structure is also reflected by the bathymetry. Figure 12 shows three along-axis profiles of bathymetry, located on the ridge axis and at $\pm$7 km across-axis distance, respectively. The profiles on axis and at 7 km across-axis distance show a steeper decline on the east side of the segment center, whereas the profile at $-$7 km across-axis distance shows a symmetrical variation, probably due to the presence of an inside corner and an outside corner on the west and east sides, respectively. A similar asymmetry is also observed on the MBA map [*Sauter et al.*, 2001]. This asymmetry in the thermal structure begins at $<$5 km distance away from the magma chamber, suggesting a rapid cooling mechanism on the east side of the magma chamber.

Recently, *Hasenclever et al.* [2014] performed numerical modeling to reproduce the seismic structure of an axial magma chamber at the fast-spreading East Pacific Rise [*Dunn et al.*, 2000]. They demonstrated that the hydrothermal circulation penetrating the lower crust is required, which has also been suggested by the observations of ophiolite [*VanTongeren et al.*, 2008; *Nicolas et al.*, 2003, 2015]. The deep-penetrating hydrothermal circulation is shaped by the geometry of the brittle-ductile layer (also used as a permeability boundary in the modeling), recharged through the off-axis pervasive flow and discharged on axis, accounting for about 70% of the heat released on axis. *Dunn et al.* [2013] also suggested that deep-penetrating circulation is required to explain the variation of the across-axis width variation of the magma system along the East Lau spreading center. On the other hand, recent microearthquake observations and numerical modeling suggested that the hydrothermal circulation cells may favor an along-axis orientation as the axial region corresponds to a high-permeability band [*Tolstoy et al.*, 2008; *Crawford et al.*, 2013; *Fontaine et al.*, 2014; *Coumou et al.*, 2008]. In addition, the along-axis slope of the brittle-ductile boundary at slow/ultraslow ridges may help the development of large-size along-axis circulation cells by focusing the upwelling flow to the summit of this boundary [*Fontaine et al.*, 2008]. By integrating these ideas, we propose that the thick fractured crust on the east side of the segment center may act as a high-permeability layer to allow along-axis, deep-penetrating hydrothermal circulation to develop and cool the mid to lower crust.

The development of such features should rely on several factors that are specific to the ultraslow-spreading environment, including the narrowness of the magmatic center, the wide axial weakness zone, and the rapid change from orthogonal to oblique spreading. By providing additional recharging flows, it would eventually enhance the efficiency of ultraslow ridges in supporting hydrothermal vent fields, consistent with the hydrothermal plume observations [*Baker et al.*, 2004]. Additionally, *Cannat et al.* [2008] speculated that the oblique spreading affects crustal accretion by impeding the lateral dyke propagation via limiting the width of weakness zones or increasing the thickness of the lithosphere. We propose that due to the development of the along-axis hydrothermal circulation, the modification of the oblique spreading on the thermal structure would fundamentally affect all the crustal processes.

## 7. Conclusions

We have presented a 3-D seismic velocity structure from the seafloor down to the Moho at the SWIR segment 27. It contains a very thick crust and a lower crustal low-velocity anomaly, which are significantly different from the previous seismic images at other ultraslow-spreading ridge segments.

The PmP-determined crustal thickness is very thick at the segment center (~9.5 km) and thins to <7 km toward the segment ends. The thick crust as well as the robust melt supply at the segment center can be traced off axis to at least 3 Ma. It is ascribed to the enhanced focusing mechanism under the ultraslow-spreading environment [*Li et al.*, 2015].

The upper crust is a brittle layer characterized by decreased velocities, high vertical velocity gradients, and azimuthal anisotropy. The velocity is even lower around the ridge axis. These observations are related to the porosity induced by tectonic fracturing and faulting in the median valley, and the increase in velocity may be due to the hydrothermal precipitation in the aged crust and the closure of pore space at depth. The fast direction of the anisotropy indicates that the cracks are vertically aligned and subperpendicular to the spreading

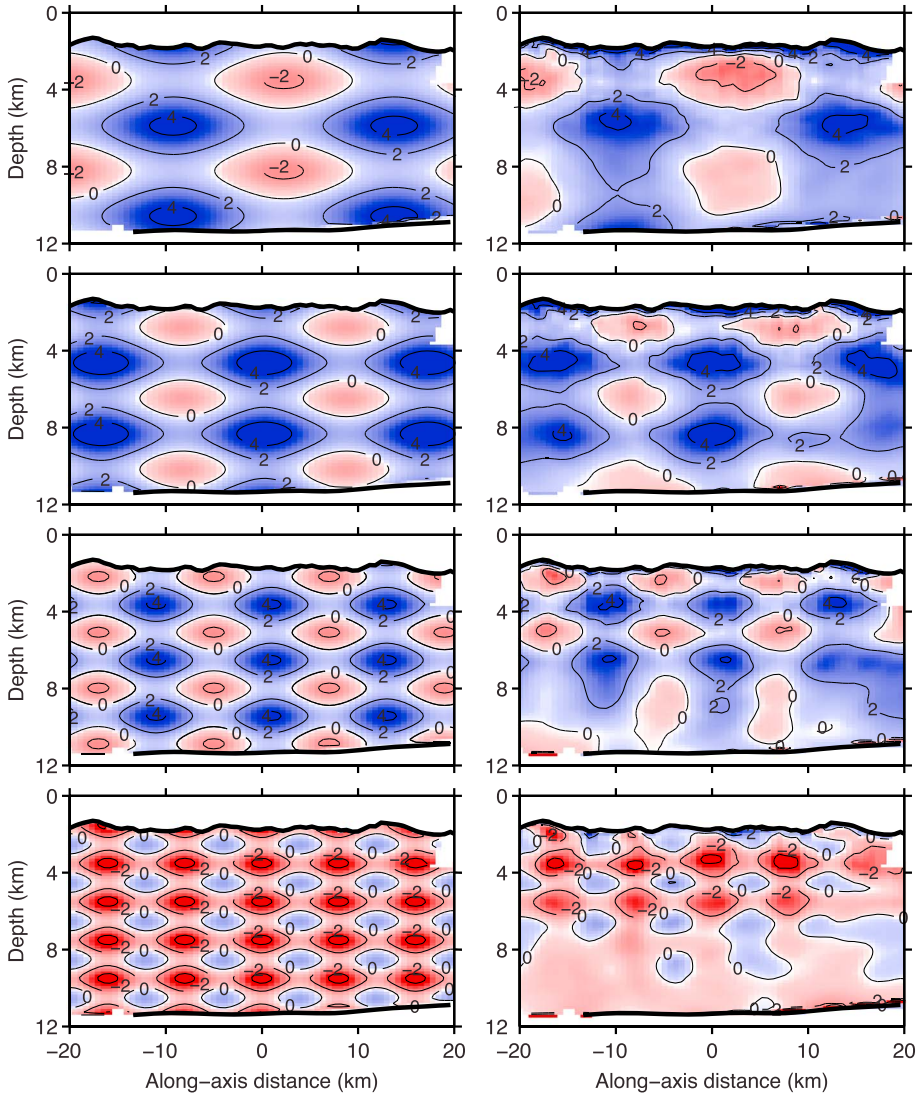


**Figure A1.** Checkerboard tests. On the left column is the input pattern, whereas on the right is the output. The contours and numbers represent the perturbations in percent. The four rows correspond to four different patterns. The cross section is running across the segment center perpendicularly to the ridge axis. The tests indicate that the 3-D tomography is able to recover anomalies with size of about 5 km horizontally by 2 km vertically at the center of the model.

direction, rather than parallel to the ridge axis trend. The thickness of layer 2 is 3–3.5 km at the segment center and on its west side, but gradually increases to the crustal thickness (~7 km) at 20 km away on the east side.

In the lower crust, we image a round-shaped low-velocity anomaly between 4 and 5 km bsf and the Moho depth. The maximum velocity anomaly is −0.6 km/s as compared to the off-axis velocity, suggesting the presence of a small amount of melt. The low-velocity anomaly represents a crustal magma chamber that is localized beneath the segment center.

At midcrustal depth, we observe a small low-velocity anomaly on the west side of the segment center and interpret it as evidence for lateral magma redistribution. On the east side, the deep-penetrating high velocity gradients suggest an intensely fractured cold crust existing close to the segment center. The asymmetry is explained by an along-axis deep-penetrating hydrothermal circulation system, that develops in response to the rapid change from orthogonal to oblique spreading on the east side of the segment center. This system would modify the thermal structure and eventually affect all the crustal processes.

## Appendix A: Checkerboard Tests

We examined the resolvability of the 3-D velocity model with checkerboard tests. The source and receiver geometry for the synthetic tests is the same as for the real-data inversion. We created the input model by

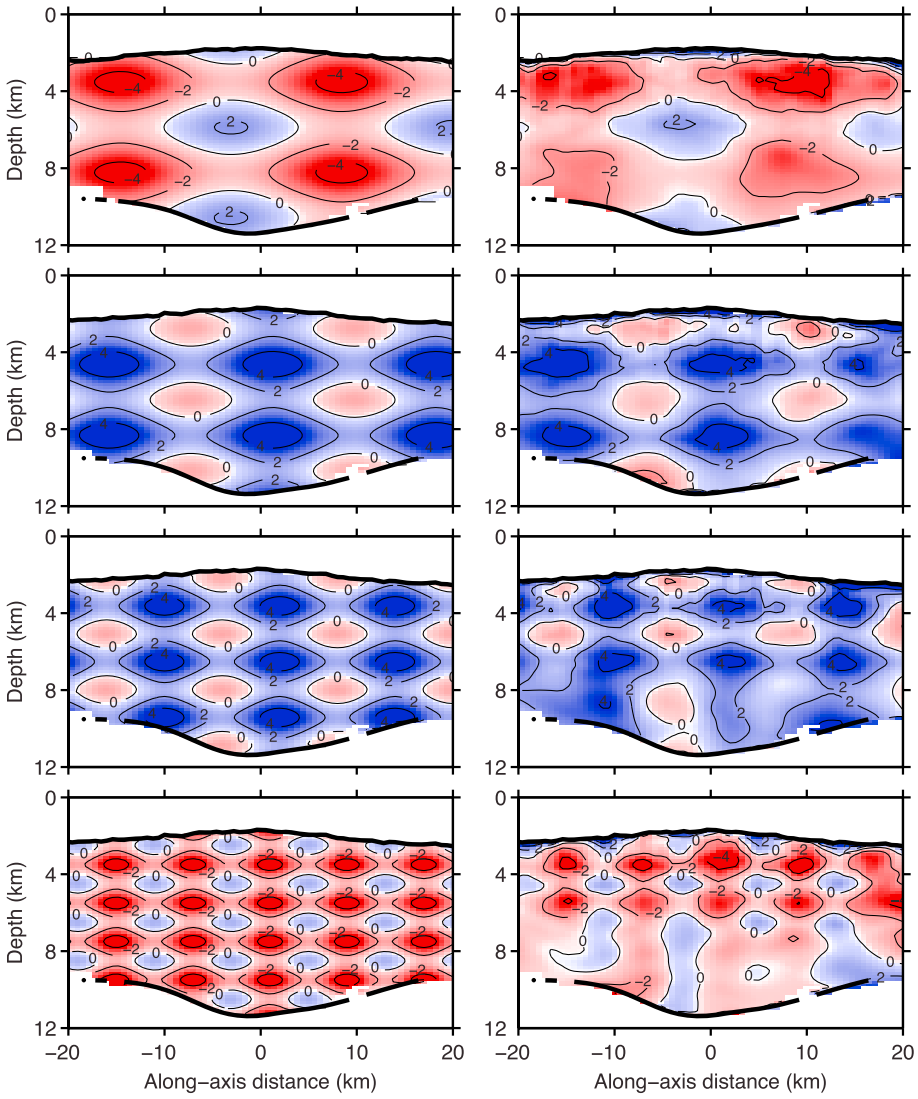


**Figure A2.** Checkerboard tests. Same as Figure A1, except for the profile running along the ridge axis.

adding a checkerboard pattern to the smoothed final model. The pattern is characterized by a wavelength for the two horizontal dimensions ($\lambda_h$) and a vertical wavelength ($\lambda_v$). The three sinusoidal functions were summed up for a 3-D pattern. Synthetic data was created with the forward modeling engine in the tomography code. Then it was inverted from the same starting model and in the same routine as for the real-data inversion (the standard solution). The input and inverted models are compared along the cross-sections running over the segment center perpendicularly to (Figure A1) and along the ridge axis (Figure A2).

We tested four patterns with different wavelengths ranging between 23 km and 8 km horizontally, and 4.7 km and 2 km vertically. In all the tests, velocities in the shallowest 0.3 km are overestimated due to the lack of turning ray path and the dominance of smoothing constraints over damping constraints in the inversion. The patterns above ~8 km bsl (6–6.5 km bsf) are well resolved in all the tests, corresponding to the highest data coverage. Below that, only the long-wavelength patterns ($\lambda_h/2 \geq 8.5$ km and $\lambda_v/2 \geq 1.9$ km) can be resolved.

**Acknowledgments**

We thank the Captain and the crew of R/V *Dayang Yihao* for their efforts to complete the first Chinese active-source 3-D OBS experiment in February 2010. We equally thank the onboard scientific party and OBS groups. We are very grateful to Alistair J. Harding for providing the tomography code. We thank two anonymous reviewers for thoughtful reviews. Institut de Physique du Globe de Paris and ITAG, Peking University provided CPU clusters for this study. Part of the figures is created using Seismic Unix and GMT [*Wessel et al.*, 2013]. COMRA provided the ship time of R/V *Dayang Yihao* to conduct the OBS experiment. This work was supported by MOST grant (2012CB417301), COMRA grant (DYXM-115-02-3-01), and NSF China grant (41030857). The inversion results and data used to generate figures are available upon request via e-mail to the corresponding author. Institut de Physique du Globe de Paris contribution 3807.

## References

Ao, W., M. Zhao, X. Qiu, J. Li, A. Ruan, S. Li, and J. Zhang (2010), The correction of shot and OBS position in the 3D seismic experiment of the SW Indian Ocean Ridge, *Chin. J. Geophys.*, *53*(6), 1072–1081.

Arai, R., and R. A. Dunn (2014), Seismological study of Lau back arc crust: Mantle water, magmatic differentiation, and a compositionally zoned basin, *Earth Planet. Sci. Lett.*, *390*, 304–317.

Arnulf, A., S. Singh, A. Harding, G. Kent, and W. Crawford (2011), Strong seismic heterogeneity in layer 2A near hydrothermal vents at the Mid-Atlantic Ridge, *Geophys. Res. Lett.*, *38*, L13320, doi:10.1029/2011GL047753.

Artemieva, I. M., and H. Thybo (2013), EUNAseis: A seismic model for Moho and crustal structure in Europe, Greenland, and the North Atlantic Region, *Tectonophysics*, *609*, 97–153, doi:10.1016/j.tecto.2013.08.004.

Baker, E. T. (2009), Relationships between hydrothermal activity and axial magma chamber distribution, depth, and melt content, *Geochem. Geophys. Geosyst.*, *10*, Q06009, doi:10.1029/2009GC002424.

Baker, E. T., H. N. Edmonds, P. J. Michael, W. Bach, H. J. B. Dick, J. E. Snow, S. L. Walker, N. R. Banerjee, and C. H. Langmuir (2004), Hydrothermal venting in magma deserts: The ultraslow-spreading Gakkel and Southwest Indian ridges, *Geochem. Geophys. Geosyst.*, *5*, Q08002, doi:10.1029/2004GC000712.

Barclay, A. H., D. R. Toomey, and S. C. Solomon (1998), Seismic structure and crustal magmatism at the Mid-Atlantic Ridge, 35°, *J. Geophys. Res.*, *103*(B8), 17,827–17,844.

Barclay, A. H., D. R. Toomey, and S. C. Solomon (2001), Microearthquake characteristics and crustal Vp/Vs structure at the Mid-Atlantic Ridge, 35°N, *J. Geophys. Res.*, *106*(B2), 2017–2034.

Bazin, S., A. Harding, G. Kent, J. Orcutt, C. Tong, J. Pye, S. Singh, P. Barton, M. Sinha, and R. White (2001), Three-dimensional shallow crustal emplacement at the 9°03′N overlapping spreading center on the East Pacific Rise: Correlations between magnetization and tomographic images, *J. Geophys. Res.*, *106*(B8), 16,101–16,117.

Berryman, J. G., S. R. Pride, and H. F. Wang (2002), A differential scheme for elastic properties of rocks with dry or saturated cracks, *Geophys. J. Int.*, *151*(2), 597–611.

Bonatti, E., J. R. Lawrence, and N. Morandi (1984), Serpentinization of oceanic peridotites: Temperature dependence of mineralogy and boron content, *Earth Planet. Sci. Lett.*, *70*(1), 88–94.

Bown, J. W., and R. S. White (1994), Variation with spreading rate of oceanic crustal thickness and geochemistry, *Earth Planet. Sci. Lett.*, *121*(3), 435–449.

Canales, J. P., R. S. Detrick, J. Lin, J. A. Collins, and D. R. Toomey (2000a), Crustal and upper mantle seismic structure beneath the rift mountains and across a nontransform offset at the Mid-Atlantic Ridge (35°n), *J. Geophys. Res.*, *105*(B2), 2699–2719, doi:10.1029/1999JB900379.

Canales, J. P., J. A. Collins, J. Escartin, and R. S. Detrick (2000b), Seismic structure across the rift valley of the Mid-Atlantic Ridge at 23°20′ (MARK area): Implications for crustal accretion processes at slow spreading ridges, *J. Geophys. Res.*, *105*(B12), 28,411–28,425, doi:10.1029/2000JB900301.

Cannat, M., C. Rommevaux-Jestin, D. Sauter, C. Deplus, and V. Mendel (1999), Formation of the axial relief at the very slow spreading Southwest Indian Ridge (49° to 69°E), *J. Geophys. Res.*, *104*(B10), 22,825–22,843.

Cannat, M., D. Sauter, V. Mendel, E. Ruellan, K. Okino, J. Escartin, V. Combier, and M. Baala (2006), Modes of seafloor generation at a melt-poor ultraslow-spreading ridge, *Geology*, *34*(7), 605–608, doi:10.1130/g22486.1.

Cannat, M., D. Sauter, A. Bezos, C. Meyzen, E. Humler, and M. Le Rigoleur (2008), Spreading rate, spreading obliquity, and melt supply at the ultraslow spreading Southwest Indian Ridge, *Geochem. Geophys. Geosyst.*, *9*, Q04002, doi:10.1029/2007GC001676.

Carbotte, S. M., M. Marjanovic, H. Carton, J. C. Mutter, J. P. Canales, M. R. Nedimovic, S. S. Han, and M. R. Perfit (2013), Fine-scale segmentation of the crustal magma reservoir beneath the East Pacific Rise, *Nat. Geosci.*, *6*(10), 866–870, doi:10.1038/ngeo1933.

Carbotte, S. M., D. K. Smith, M. Cannat, and E. M. Klein (2015), Tectonic and magmatic segmentation of the Global Ocean Ridge System: A synthesis of observations, *Geol. Soc. London Spec. Publ.*, *420*, 249–295.

Carlson, R. (1998), Seismic velocities in the uppermost oceanic crust: Age dependence and the fate of layer 2A, *J. Geophys. Res.*, *103*(B4), 7069–7077.

Chen, Y. J. (1992), Oceanic crustal thickness versus spreading rate, *Geophys. Res. Lett.*, *19*(8), 753–756, doi:10.1029/92GL00161.

Christensen, N. I. (1979), Compressional wave velocities in rocks at high temperatures and pressures, critical thermal gradients, and crustal low-velocity zones, *J. Geophys. Res.*, *84*(B12), 6849–6857.

Coumou, D., T. Driesner, and C. Heinrich (2008), The structure and dynamics of mid-ocean ridge hydrothermal systems, *Science*, *321*(5897), 1825–1828.

Crawford, W. C., A. Rai, S. C. Singh, M. Cannat, J. Escartin, H. Wang, R. Daniel, and V. Combier (2013), Hydrothermal seismicity beneath the summit of Lucky Strike volcano, Mid-Atlantic Ridge, *Earth Planet. Sci. Lett.*, *373*, 118–128.

Creager, K. C., and L. M. Dorman (1982), Location of instruments on the seafloor by joint adjustment of instrument and ship positions, *J. Geophys. Res.*, *87*(B10), 8379–8388.

Curewitz, D., K. Okino, M. Asada, B. Baranov, E. Gusev, and K. Tamaki (2010), Structural analysis of fault populations along the oblique, ultra-slow spreading Knipovich Ridge, North Atlantic ocean, 74°30′n-77°50′n, *J. Struct. Geol.*, *32*(6), 727–740.

DeMets, C., R. G. Gordon, D. F. Argus, and S. Stein (1994), Effect of recent revisions to the geomagnetic reversal time scale on estimates of current plate motions, *Geophys. Res. Lett.*, *21*(20), 2191–2194, doi:10.1029/94GL02118.
DeMets, C., S. Merkouriev, and D. Sauter (2015), High-resolution estimates of Southwest Indian Ridge plate motions, 20 Ma to present, *Geophys. J. Int.*, *203*(3), 1495–1527.
Detrick, R., J. Collins, R. Stephen, and S. Swift (1994), In situ evidence for the nature of the seismic layer 2/3 boundary in oceanic crust, *Nature*, *370*(6487), 288–290.
Detrick, R. S., R. S. White, and G. M. Purdy (1993), Crustal structure of North Atlantic fracture zones, *Acta Crystallogr.*, *31*(4), 439–458.
Dick, H. J. B., J. Lin, and H. Schouten (2003), An ultraslow-spreading class of ocean ridge, *Nature*, *426*(6965), 405–412, doi:10.1038/nature02128.
Dunn, R. A. (2015), Tracking stress and hydrothermal activity along the Eastern Lau Spreading Center using seismic anisotropy, *Earth Planet. Sci. Lett.*, *410*, 105–116.
Dunn, R. A., D. R. Toomey, and S. C. Solomon (2000), Three-dimensional seismic structure and physical properties of the crust and shallow mantle beneath the East Pacific Rise at 9°30'N, *J. Geophys. Res.*, *105*, 23,537–23,555.
Dunn, R. A., V. Lekic, R. S. Detrick, and D. R. Toomey (2005), Three-dimensional seismic structure of the Mid-Atlantic Ridge (35°N): Evidence for focused melt supply and lower crustal dike injection, *J. Geophys. Res.*, *110*, B09101, doi:10.1029/2004JB003473.
Dunn, R. A., F. Martinez, and J. A. Conder (2013), Crustal construction and magma chamber properties along the Eastern Lau Spreading Center, *Earth Planet. Sci. Lett.*, *371*, 112–124.
Dziak, R. P., C. G. Fox, and A. E. Schreiner (1995), The June–July 1993 seismo-acoustic event at coaxial segment, Juan de Fuca Ridge: Evidence for a lateral dike injection, *Geophys. Res. Lett.*, *22*(22), 135–138.
Eason, D. E., and R. A. Dunn (2015), Petrogenesis and structure of oceanic crust in the Lau Back-Arc Basin, *Earth Planet. Sci. Lett.*, *429*, 128–138.
Escartin, J., M. Cannat, G. Pouliquen, A. Rabain, and J. Lin (2001), Crustal thickness of V-shaped ridges south of the Azores: Interaction of the Mid-Atlantic Ridge (36–39°N) and the Azores hot spot, *J. Geophys. Res.*, *106*(B10), 21,719–21,735.
Fontaine, F. J., M. Cannat, and J. Escartin (2008), Hydrothermal circulation at slow-spreading mid-ocean ridges: The role of along-axis variations in axial lithospheric thickness, *Geology*, *36*(10), 759–762.
Fontaine, F. J., M. Cannat, J. Escartin, and W. C. Crawford (2014), Along-axis hydrothermal flow at the axis of slow spreading mid-ocean ridges: Insights from numerical models of the Lucky Strike vent field (MAR), *Geochem. Geophys. Geosyst.*, *15*, 2918–2931, doi:10.1002/2014GC005372.
Harding, A., J. Orcutt, M. Kappus, E. Vera, J. Mutter, P. Buhl, R. Detrick, and T. Brocher (1989), Structure of young oceanic crust at 13°N on the East Pacific Rise from expanding spread profiles, *J. Geophys. Res.*, *94*(B9), 12,163–12,196, doi:10.1029/JB094iB09p12163.
Harding, A. J., G. M. Kent, and J. A. Orcutt (1993), A multichannel seismic investigation of upper crustal structure at 9°N on the East Pacific Rise—Implications for crustal accretion, *J. Geophys. Res.*, *98*(B8), 13,925–13,944, doi:10.1029/93JB00886.
Hasenclever, J., S. Theissen-Krah, L. H. Rüpke, J. P. Morgan, K. Iyer, S. Petersen, and C. W. Devey (2014), Hybrid shallow on-axis and deep off-axis hydrothermal circulation at fast-spreading ridges, *Nature*, *508*(7497), 508–512.
Hobro, J. W. D., S. C. Singh, and T. A. Minshull (2003), Three-dimensional tomographic inversion of combined reflection and refraction seismic traveltime data, *Geophys. J. Int.*, *152*(1), 79–93, doi:10.1046/j.1365-246X.2003.01822.x.
Hooft, E. E. E., R. S. Detrick, D. R. Toomey, J. A. Collins, and J. Lin (2000), Crustal thickness and structure along three contrasting spreading segments of the Mid-Atlantic Ridge, 33.5°–35°N, *J. Geophys. Res.*, *105*(B4), 8205–8226, doi:10.1029/1999JB900442.
Hosford, A., J. Lin, and R. S. Detrick (2001), Crustal evolution over the last 2 m.y. at the Mid-Atlantic Ridge OH-1 segment, 35°N, *J. Geophys. Res.*, *106*(B7), 13,269–13,286.
Hung, S.-H., F. Dahlen, and G. Nolet (2000), Fréchet kernels for finite-frequency travel times II. Examples, *Geophys. J. Int.*, *141*(1), 175–203.
Jokat, W., and M. C. Schmidt-Aursch (2007), Geophysical characteristics of the ultraslow spreading Gakkel Ridge, Arctic Ocean, *Geophys. J. Int.*, *168*(3), 983–998.
Jokat, W., J. Kollofrath, W. H. Geissler, and L. Jensen (2012), Crustal thickness and earthquake distribution south of the Logachev Seamount, Knipovich Ridge, *Geophys. Res. Lett.*, *39*, L08302, doi:10.1029/2012GL051199.
Karato, S.-i (1993), Importance of anelasticity in the interpretation of seismic tomography, *Geophys. Res. Lett.*, *20*(15), 1623–1626.
Kent, G. M., S. C. Singh, A. J. Harding, M. C. Sinha, J. A. Orcutt, P. J. Barton, R. S. White, S. Bazin, R. W. Hobbs, C. H. Tong, and J. W. Pye (2000), Evidence from three-dimensional seismic reflectivity images for enhanced melt supply beneath mid-ocean-ridge discontinuities, *Nature*, *406*(6796), 614–618, doi:10.1038/35020543.
Korenaga, J., W. Holbrook, G. Kent, P. Kelemen, R. Detrick, H.-C. Larsen, J. Hopper, and T. Dahl-Jensen (2000), Crustal structure of the Southeast Greenland Margin from joint refraction and reflection seismic tomography, *J. Geophys. Res.*, *105*(B9), 21,591–21,614.
Li, J., et al. (2015), Seismic observation of an extremely magmatic accretion at the ultraslow spreading Southwest Indian Ridge, *Geophys. Res. Lett.*, *42*, 2656–2663, doi:10.1002/2014GL062521.
Lin, J., G. Purdy, H. Schouten, J. Sempere, and C. Zervas (1990), Evidence from gravity data for focused magmatic accretion along the Mid-Atlantic Ridge, *Nature*, *344*(6267), 627–632.
Macdonald, K. C., P. J. Fox, L. J. Perram, M. F. Eisen, R. M. Haymon, S. P. Miller, S. M. Carbotte, M. H. Cormier, and A. N. Shor (1988), A new view of the mid-ocean ridge from the behavior of ridge-axis discontinuities, *Nature*, *335*(6187), 217–225, doi:10.1038/335217a0.
Magde, L. S., A. H. Barclay, D. R. Toomey, R. S. Detrick, and J. A. Collins (2000), Crustal magma plumbing within a segment of the mid-atlantic ridge, 35°N, *Earth Planet. Sci. Lett.*, *175*(1), 55–67.
McCaughey, M., and S. C. Singh (1997), Simultaneous velocity and interface tomography of normal-incidence and wide-aperture seismic traveltime data, *Geophys. J. Int.*, *131*(1), 87–99.
Mendel, V., and D. Sauter (1997), Seamount volcanism at the super slow-spreading Southwest Indian Ridge between 57°E and 70°E, *Geology*, *25*(2), 99–102.
Mendel, V., D. Sauter, L. Parson, and J.-R. Vanney (1997), Segmentation and morphotectonic variations along a super slow-spreading center: The Southwest Indian Ridge (57°E–70°E), *Mar. Geophys. Res.*, *19*(6), 505–533.
Minshull, T. A., M. R. Muller, C. J. Robinson, R. S. White, and M. J. Bickle (1998), Is the oceanic Moho a serpentinization front?, *Geol. Soc. London Spec. Publ.*, *148*(1), 71–80.
Minshull, T. A., M. R. Muller, and R. S. White (2006), Crustal structure of the Southwest Indian Ridge at 66°E: Seismic constraints, *Geophys. J. Int.*, *166*(1), 135–147, doi:10.1111/j.1365-246X.2006.03001.x.
Morgan, J. P., and Y. J. Chen (1993), Genesis of oceanic crust: Magma injection, hydrothermal circulation, and crustal flow, *J. Geophys. Res.*, *98*(B4), 6283–6298.
Moser, T. (1991), Shortest path calculation of seismic rays, *Geophysics*, *56*(1), 59–67.

Muller, M. R., C. J. Robinson, T. A. Minshull, R. S. White, and M. J. Bickle (1997), Thin crust beneath ocean drilling program borehole 735B at the Southwest Indian Ridge?, *Earth Planet. Sci. Lett.*, *148*(1), 93–107.

Nicolas, A., D. Mainprice, and F. Boudier (2003), High-temperature seawater circulation throughout crust of oceanic ridges: A model derived from the Oman ophiolites, *J. Geophys. Res.*, *108*(B8), 2371, doi:10.1029/2002JB002094.

Nicolas, A., F. Boudier, and D. Mainprice (2015), Paragenesis of magma chamber internal wall discovered in Oman ophiolite gabbros, *Terra Nova*, *28*, 91–100.

Niu, X., A. Ruan, J. Li, T. Minshull, D. Sauter, Z. Wu, X. Qiu, M. Zhao, Y. J. Chen, and S. Singh (2015), Along-axis variation in crustal thickness at the ultraslow spreading Southwest Indian Ridge (50°E) from a wide-angle seismic experiment, *Geochem. Geophys. Geosyst.*, *16*, 468–485, doi:10.1002/2014GC005645.

Paige, C. C., and M. A. Saunders (1982), LSQR: An algorithm for sparse linear equations and sparse least squares, *ACM Trans. Math. Software*, *8*(1), 43–71.

Purdy, G. M. (1982), The correction for the travel time effects of seafloor topography in the interpretation of marine seismic data, *J. Geophys. Res.*, *87*(B10), 8389–8396, doi:10.1029/JB087iB10p08389.

Reid, I., and H. Jackson (1981), Oceanic spreading rate and crustal thickness, *Mar. Geophys. Res.*, *5*(2), 165–172.

Rommevaux-Jestin, C., C. Deplus, and P. Patriat (1997), Mantle Bouguer anomaly along an ultra slow-spreading ridge: Implications for accretionary processes and comparison with results from central Mid-Atlantic Ridge, *Mar. Geophys. Res.*, *19*(6), 481–503.

Ryan, M. P., R. Y. Koyanagi, and R. S. Fiske (1981), Modeling the three-dimensional structure of macroscopic magma transport systems: Application to Kilauea volcano, Hawaii, *J. Geophys. Res.*, *86*(86), 7111–7129.

Sauter, D., and M. Cannat (2010), The ultraslow spreading Southwest Indian Ridge, in *Diversity of Hydrothermal Systems on Slow Spreading Ocean Ridges*, pp. 153–173, AGU, Washington, D. C.

Sauter, D., P. Patriat, C. Rommevaux-Jestin, M. Cannat, and A. Briais (2001), The Southwest Indian Ridge between 49°15′E and 57°E: Focused accretion and magma redistribution, *Earth Planet. Sci. Lett.*, *192*(3), 303–317.

Sauter, D., et al. (2002), TOBI sidescan sonar imagery of the very slow-spreading Southwest Indian Ridge: Evidence for along-axis magma distribution, *Earth Planet. Sci. Lett.*, *199*(1), 81–95.

Sauter, D., H. Carton, V. Mendel, M. Munschy, C. Rommevaux-Jestin, J.-J. Schott, and H. Whitechurch (2004), Ridge segmentation and the magnetic structure of the Southwest Indian Ridge (at 50°30′E, 55°30′E and 66°20′E): Implications for magmatic processes at ultraslow-spreading centers, *Geochem. Geophys. Geosyst.*, *5*, Q05K08, doi:10.1029/2003GC000581.

Sauter, D., M. Cannat, C. Meyzen, A. Bezos, P. Patriat, E. Humler, and E. Debayle (2009), Propagation of a melting anomaly along the ultraslow Southwest Indian Ridge between 46°E and 52°20′E: Interaction with the Crozet hotspot?, *Geophys. J. Int.*, *179*(2), 687–699, doi:10.1111/j.1365-246X.2009.04308.x.

Sauter, D., M. Cannat, S. Roumejon, M. Andreani, D. Birot, A. Bronner, D. Brunelli, J. Carlut, A. Delacour, and V. Guyader (2013), Continuous exhumation of mantle-derived rocks at the Southwest Indian Ridge for 11 million years, *Nat. Geosci.*, *6*(4), 314–320.

Seher, T., W. C. Crawford, S. C. Singh, M. Cannat, V. Combier, and D. Dusunur (2010a), Crustal velocity structure of the Lucky Strike segment of the Mid-Atlantic Ridge at 37°N from seismic refraction measurements, *J. Geophys. Res.*, *115*, B03103, doi:10.1029/2009JB006650.

Seher, T., S. C. Singh, W. C. Crawford, and J. Escartin (2010b), Upper crustal velocity structure beneath the central Lucky Strike segment from seismic refraction measurements, *Geochem. Geophys. Geosyst.*, *11*, Q05001, doi:10.1029/2009GC002894.

Shaw, P. R., and J. A. Orcutt (1985), Waveform inversion of seismic refraction data and applications to young Pacific crust, *Geophys. J. R. Astron. Soc.*, *82*(3), 375–414.

Singh, S. C., W. C. Crawford, H. Carton, T. Seher, V. Combier, M. Cannat, J. P. Canales, D. Duesuenuer, J. Escartin, and J. M. Miranda (2006), Discovery of a magma chamber and faults beneath a Mid-Atlantic Ridge hydrothermal field, *Nature*, *442*(7106), 1029–1032, doi:10.1038/nature05105.

Tao, C. H., J. Lin, S. Q. Guo, Y. J. Chen, G. H. Wu, X. Q. Han, C. R. German, D. R. Yoerger, N. Zhou, H. M. Li, X. Su, J. Zhu, and the DY115-19 (Legs 1-2), and the DY115-20 (Legs 4-7) Science Parties (2012), First active hydrothermal vents on an ultraslow-spreading center: Southwest Indian Ridge, *Geology*, *40*(1), 47–50, doi:10.1130/g32389.1.

Tolstoy, M., F. Waldhauser, D. Bohnenstiehl, R. Weekly, and W.-Y. Kim (2008), Seismic identification of along-axis hydrothermal flow on the East Pacific Rise, *Nature*, *451*(7175), 181–184.

Toomey, D. R., S. C. Solomon, and G. Purdy (1994), Tomographic imaging of the shallow crustal structure of the East Pacific Rise at 9°30′N, *J. Geophys. Res.*, *99*(B12), 24,135–24,157.

Tuckwell, G., J. Bull, and D. Sanderson (1998), Numerical models of faulting at oblique spreading centers, *J. Geophys. Res.*, *103*(B7), 15,473–15,482.

Van Avendonk, H. J. A., A. J. Harding, J. A. Orcutt, and J. S. McClain (1998), A two-dimensional tomographic study of the Clipperton transform fault, *J. Geophys. Res.*, *103*(B8), 17,885–17,899, doi:10.1029/98JB00904.

Van Avendonk, H. J. A., D. J. Shillington, W. S. Holbrook, and M. J. Hornbach (2004), Inferring crustal structure in the Aleutian island arc from a sparse wide-angle seismic data set, *Geochem. Geophys. Geosyst.*, *5*, Q08008, doi:10.1029/2003GC000664.

VanTongeren, J. A., P. B. Kelemen, and K. Hanghøj (2008), Cooling rates in the lower crust of the Oman ophiolite: Ca in olivine, revisited, *Earth Planet. Sci. Lett.*, *267*(1), 69–82.

Vera, E. E., J. C. Mutter, P. Buhl, J. A. Orcutt, A. J. Harding, M. E. Kappus, R. S. Detrick, and T. M. Brocher (1990), The structure of 0- to 0.2-m.y.-old oceanic crust at 9°N on the East Pacific Rise from expanded spread profiles, *J. Geophys. Res.*, *95*(B10), 15,529–15,556.

Weekly, R. T., W. S. D. Wilcock, E. E. E. Hooft, D. R. Toomey, P. R. Mcgill, and D. S. Stakes (2013), Termination of a 6 year ridge-spreading event observed using a seafloor seismic network on the endeavour segment, Juan de Fuca Ridge, *Geochem. Geophys. Geosyst.*, *14*, 1375–1398, doi:10.1002/ggge.20105.

Weekly, R. T., W. S. D. Wilcock, D. R. Toomey, E. E. E. Hooft, and E. Kim (2014), Upper crustal seismic structure of the endeavour segment, Juan de Fuca Ridge from traveltime tomography: Implications for oceanic crustal accretion, *Geochem. Geophys. Geosyst.*, *15*, 1296–1315, doi:10.1002/2013GC005159.

Wessel, P., W. H. Smith, R. Scharroo, J. Luis, and F. Wobbe (2013), Generic mapping tools: Improved version released, *Eos Trans. AGU*, *94*(45), 409–410.

White, R. S., T. Minshull, M. Bickle, and C. Robinson (2001), Melt generation at very slow-spreading oceanic ridges: Constraints from geochemical and geophysical data, *J. Petrol.*, *42*(6), 1171–1196.

Xue, J., Y. Zhou, and Y. J. Chen (2015), Tomographic resolution of plume anomalies in the lowermost mantle, *Geophys. J. Int.*, *201*(2), 979–995.

Zelt, C. A. (1999), Modelling strategies and model assessment for wide-angle seismic traveltime data, *Geophys. J. Int.*, *139*(1), 183–204.

Zhao, M., X. Qiu, J. Li, D. Sauter, A. Ruan, J. Chen, M. Cannat, S. Singh, J. Zhang, and Z. Wu (2013), Three-dimensional seismic structure of the Dragon Flag oceanic core complex at the ultraslow spreading Southwest Indian Ridge (49°39′E), *Geochem. Geophys. Geosyst.*, *14*, 4544–4563, doi:10.1002/ggge.20264.

Zhou, H., and H. J. B. Dick (2013), Thin crust as evidence for depleted mantle supporting the Marion Rise, *Nature*, *494*(7436), 195–200, doi:10.1038/nature11842.